Heat flux correlation models for spray evaporative cooling of vibrating surfaces in the nucleate boiling region

Article (Accepted Version)

Heat flux correlation models for spray evaporative cooling of vibrating surfaces in the nucleate boiling region

by

A Sarmadian[a], J.F. Dunne[a*], C.A. Long[a], J. Thalackottore Jose[a], J-P Pirault[a], and Cedric Rouaud[b]

[a]Department of Engineering and Design
School of Engineering and Informatics
University of Sussex, Falmer, Brighton, BN1 9QT, UK.
*Corresponding author: E-mail: j.f.dunne@sussex.ac.uk

[b]Ricardo plc
Shoreham-by-Sea, West Sussex BN43 5FG, UK

Abstract

New empirical correlation models are constructed to characterise heat transfer associated with spray evaporative cooling of vibrating surfaces - a process involving complex two-phase physics well beyond current numerical simulation capabilities. The proposed correlation models, which account for dynamic, rather than just static surface conditions as in existing models, are constructed using dimensional analysis involving the Generalized Buckingham Π-Theorem. Experimentally-measured spray evaporative cooling data is used to fit the model using the Vibrational Reynolds number and a dimensionless acceleration number which better correlate the influence of surface frequency and amplitude in the nucleate boiling regime. Different coolant flow-rates through a full-cone spray nozzle are used to cool a flat circular test-piece acting as a horizontal surface. The test-piece surface is excited by a shaker through a range of low and high vibration frequencies and amplitudes. The results show that surface dynamic effects certainly influence nucleate boiling, but they also show that surface vibration does not have the same effect for all excess temperatures - dynamic effects can either increase or decrease heat transfer depending on the heat transfer mechanism. These new models are important for thermal management in several areas, particularly involving batteries, power electronics, and electrical machines in automotive and aerospace applications.

1 Introduction

Designing compact, efficient, and safe thermal management systems is important for the development of future low-emission electric and plug-in hybrid vehicles [1]. Improving efficiency in low-emission vehicles is of critical importance to meet regulatory targets, for example set by the EU for 2030 and beyond [2-4]. Furthermore, light-duty vehicles are expected to provide sufficient power, range, and meet the requirements of compactness and safety. Therefore, the immediate challenge is in having the capability to confidently design cooling systems with higher levels of heat flux. Obvious examples where such a need exists is in the design of thermal management systems for very compact vehicle Range Extender engines and Li-ion battery packs. This is further complicated by the fact that cooling systems in vehicles are subject to dynamic working conditions involving agitation and large amplitude vibration, which unless the physics is understood, may lead to unexpected thermal behaviour.

In recent years, there has been increasing interest in spray evaporative cooling mechanisms for different thermal management purposes [5], including high heat fluxes at low-temperature [6], and also at high-temperature [7]. Jafari et al. [8] identified promising cooling mechanisms that may be very appropriate to automotive vehicle thermal management. Spray evaporative cooling has several major advantages in comparison with single-phase forced convective cooling. First, two-phase spray evaporative cooling benefits from higher heat transfer rates, owing to the role of the latent heat transfer mechanism. This is in comparison to the sensible heat transfer mechanism associated with conventional single-phase methods. Mudawar et al. [9] have reported that a feasible thermal management system for hybrid electric vehicles should have the potential to dissipate heat in the flux range of 1.5 - 2 $\mathrm{MW/m^2}$ while the surface temperature need not exceed 125 $^{\circ}$C. In this regard, the assessment of spray cooling showed that such heat removal requirements are achievable. In addition, the capability of spray evaporative cooling covers all the extra heat removal demands induced by the downsizing of the internal combustion (IC) cylinders in conventional vehicles [10], as well as modern range extenders in future hybrid electric vehicles. Second, there is evidence to suggest that spray evaporative cooling provides a uniform temperature across all cooling surfaces, eliminating hot spots. This key aspect is vital in the thermal management of electronic components and battery stacks, where there is an essential requirement to protect against overheating [11, 12], and fires [13]. Further possible applications can be found in the cooling of highly-boosted internal combustion engines in conventional vehicles, where temperature uniformity improves knock control [8]. Moreover, spray evaporative cooling requires significantly lower mass-flow rates, and would therefore result in a substantial reduction in the required coolant mass [14, 15], and a significant reduction in pumping power [16].

Precise thermal management for the design of future cooling systems relies on a comprehensive understanding of the different flow regimes of spray evaporative cooling. Generally, the flow pattern associated with a spray, impinging on a surface, comprises: a nucleate-boiling mode, a transition, a critical heat flux (CHF), followed by transition, and a film-boiling regime [17]. In order to represent the different flow regimes, (i.e. those commonly found in the literature on spray cooling) there are two curves for boiling and quenching, each with different coordinates. A boiling curve [18] is a plot of the heat flux versus superheat temperature, i.e. the difference between the sprayed surface temperature and the coolant saturation temperature as shown in Figure1a. A quench curve [19] is the cooled-surface temperature versus time, i.e. a plot of the transient temperature associated with these regimes during the spray cooling as shown Figure1b. One critical

conclusion from these curves is that nucleate boiling is the desired regime in which to operate as far as cooling effectiveness is concerned owing to its high heat transfer rate [17].

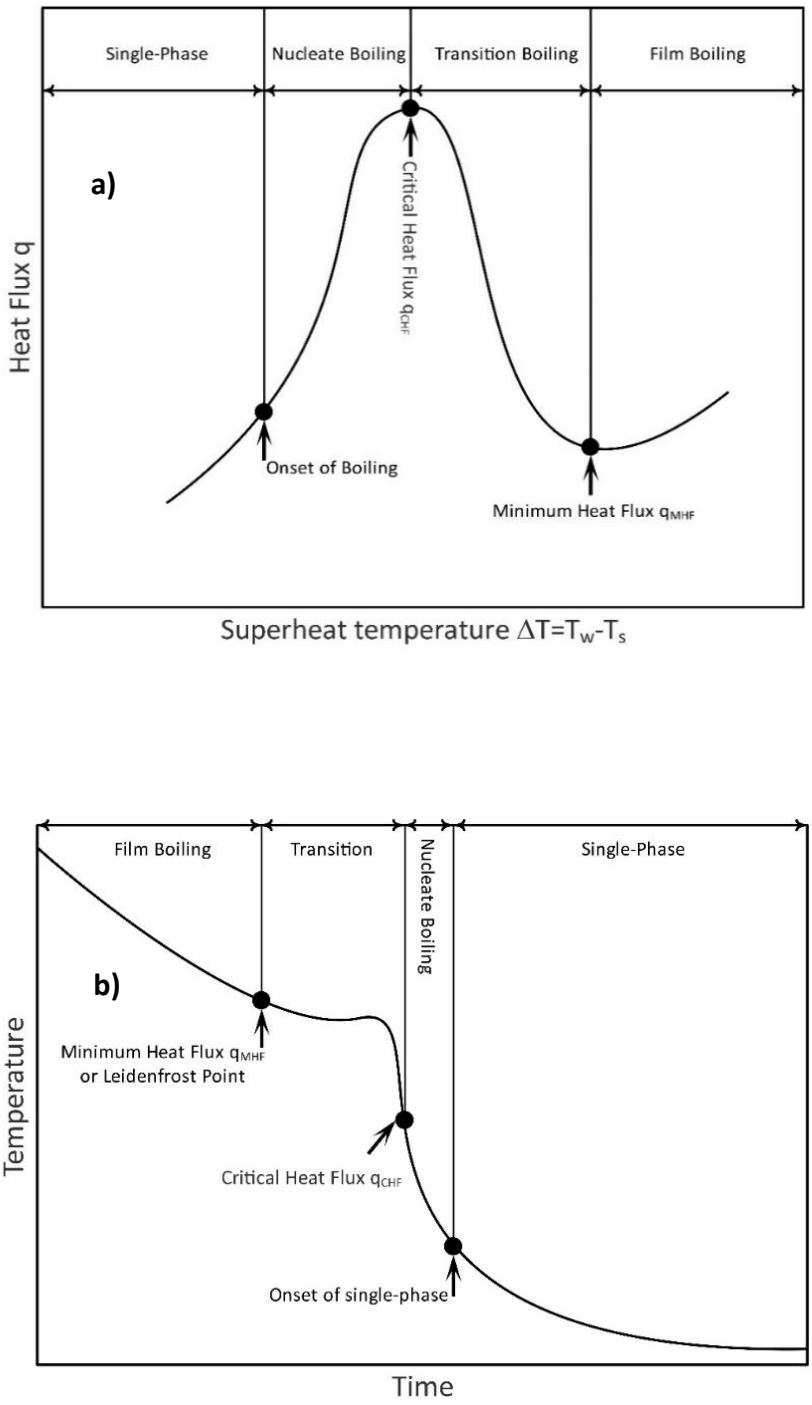

Fig. 1. Spray flow pattern maps: (a) Boiling curve, (b) Quench curve

Figure 2 demonstrates the dynamic and heat transfer mechanisms involved in the spray flow field inside a chamber (based on [20]). The working fluid first flows through the inlet pipe. It is injected by a nozzle orifice and breaks-up into droplets, flowing through the chamber until the droplets impinge on the surface. The impinged droplets accumulate, becoming larger slugs, and

move, forming a thin liquid film, or backing away from the surface, consequently splashing around. Such droplet behaviour is followed by heat removal from the hot surface through different heat transfer mechanisms. There are different heat transfer modes involved, including evaporation of the liquid film, convection in both the liquid film and the spray-flow field, as well as a droplet's effect on the liquid film. Moreover, there are two types of nucleate boiling mechanism [21]. One is a secondary nucleation generated through the interactions of impinged droplets and the thin liquid film [22]. The second is a surface nucleation stemmed from bubble generation in nucleate sites of the affected surface. These heat transfer modes, and the complexity of their resulting interactions, make developing correlations with a high nonlinearity in the heat transfer physics challenging, but of vital importance. In this regard, much of the current literature on spray cooling pays particular attention to models and empirical correlations that are important for design, such as those that can predict the interaction of the heat transfer mechanisms. Table 1 contains most of the developed correlations for nucleate boiling regime, a promising and safe mode for the design of spray cooling systems with static surfaces.

Vibration is also considered to have an influence on heat transfer [23]. Cooling systems, especially those used for the automotive industry, are mostly under dynamic environments. Consequently, modelling should consider the effect of vibration as an externally imposed force. Presently, there are no published experimental studies addressing spray cooling which involve nucleate boiling. A recent study by Sathyabhama et al. [24] investigated pool-boiling. The results of the study [7] concluded that at low frequencies (10 Hz) and amplitudes (2.5 mm), vibration has a positive influence on heat transfer coefficient (by 26%) compared to when vibration is absent. At high frequencies and amplitudes, vibration impedes boiling. This study suggests the existence of an intermediate optimum between low and high frequencies and amplitudes. For spray cooling in two-phase flow nucleate boiling, there is only one investigation involving a numerical study on the effect of single and multiple droplets on the surface in the presence of surface vibration [8]. It is performed by the *Volume of Fluid* (VOF) method [25]. The study contains two case studies of frequency injection. Low frequency injection generates a sole droplet. A slightly higher frequency injection generates less than five droplets. The whole domain contains the effect of either sole or multiple droplets on a liquid film, with a bubble sticking to the hot surface interior. A preliminary study which considers such a limited number of droplets cannot be used in modelling, thermal management, or system design of spray cooling systems, especially under dynamic conditions (e.g. automotive applications). However, it is of great importance to the theoretical understanding of the physical phenomenon. Tropea and Roisman [26] discuss that such an approach which considers such a limited number of droplets is not capable of predicting the whole spray effect behaviour reliably. They raise concern for the disturbing interactions between drops sprayed onto a surface. They also draw attention to the fluctuations that impinged droplets impose on the liquid film. The study [37] exposes a significant need for further research.

In this paper, the objective is to investigate (for the first time) the effect of vibration on spray evaporative nucleate boiling for a full-cone spray impinging on a (heated) flat circular copper test piece, driven by a shaker. Experimentally-measured data is obtained and corresponding empirical correlation models are developed and fitted by exploiting dimensional analysis and similitude conditions involving the effect of vibration on the trend of the measured data in particular making use of the Vibrational Reynolds number and a dimensionless acceleration number.

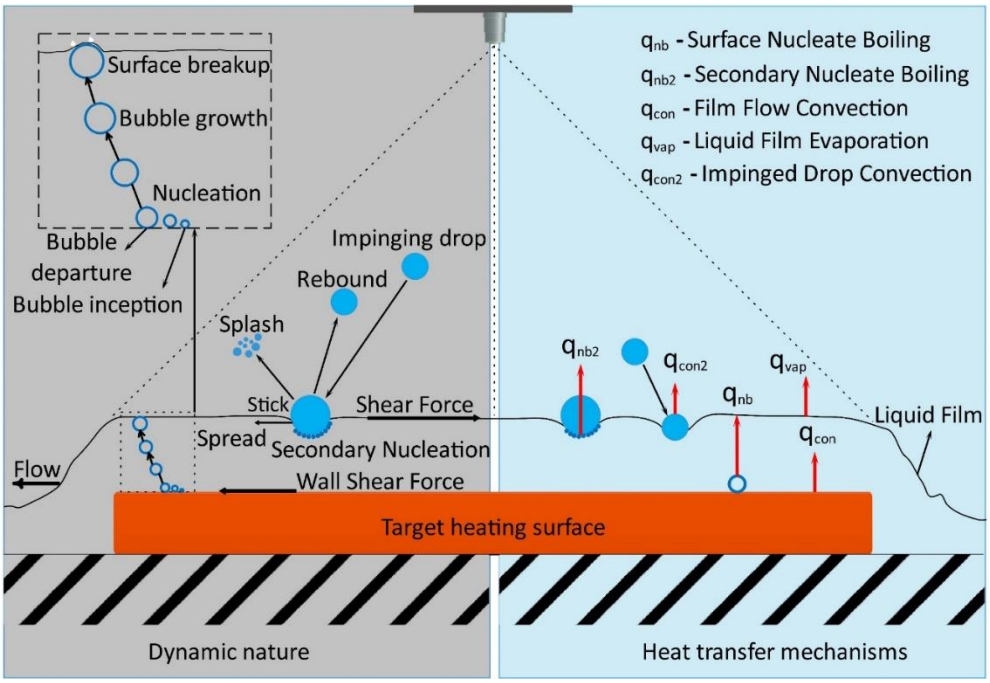

Fig. 2. Dynamic and Heat transfer characteristics of spray cooling process

Table 1. Previously undertaken studies on spray cooling in the nucleate boiling regime.

Authors	Working fluid	Only valid for: (as reported in referenced publication)	Error range of the correlations (%)	Experimental uncertainty of measured heat flux (%)	Derived experimental correlations*
Hsieh et al. (2015) [27]	**DI water**	$\Delta T_{sub} = 77\,^{\circ}C$, $We = 30$ *and* 32.9, $H = 170mm$, $Ja = 0.145 - 0.16$	± 20	5	(C1)
Yang et al. (1996) [21]	**water-air**	$d_d = 10 - 18\ \mu m$, $u_d = 25 - 58\ m/s$, $v = 0.5 - 3\ l/h$, $T_c = 20^{\circ}C$	± 4	10	(C2)
Cabrera and Gonzalez (2003) [28]	**water**	$G = 340 - 750$ kg/m^{2}s, $\Delta T_{sub} = 25 - 78\,^{\circ}C$, $R_t = 5 - 79\ \mu m$, $P_{am} = 1 - 1.8\ bar$	± 19	10	(C3)
Tan et al. (2013) [29]	**R-134a**	$q = 0.35 - 1.2\ MW/m^2$, $u_m = 18.6$ to 19.6 m/s, $d_{32} = 145$ *to* $182\ \mu m$	± 18	3.3-5.1	(C4)
Ortiz and Gonzalez (1999) [30]	**water**	Roughness levels of 320, 400, and 600 grit: $\alpha = 0 - 90$, $v = 1.5 - 3\ l/h$, $d_d = 85 - 100\ \mu m$, $T_c = 24^{\circ}C$, $\Delta T_{sub} = 30$ *and* $76\,^{\circ}C$, $q \leq 5\ MW/m^2$	± 18	≤7	(C5)
Ortiz and Gonzalez (1999) [30]	**water**	Smooth surfaces: $v = 1.5\ l/h$, $d_d = 85 - 100\ \mu m$, $T_c = 24^{\circ}C$, $\Delta T_{sub} = 30$ *and* $76\,^{\circ}C$, $q \leq 5\ MW/m^2$, P_n~5 *and* 8 *bar*	± 10	≤7	(C6)
Sehmbey et al. (1995) [31]	**Liquid N_2**	Smooth surfaces: $G = 16.9 - 88.9$ kg/m^{2}s, $d_{32} = 14 - 29\ \mu m$, $u_m =$ 14 to 30.7 m/s, $q \leq 1.65\ MW/m^2$	-	≤8	(C7)
Hsieh et al. (2004) [32]	**water**	$\Delta T_{sub} = 55 - 60\,^{\circ}C$, $We = 80 - 231$, $H = 60mm$, $d_{32} = 42 - 46\ \mu m$, $G = 0.178 - 0.306$ kg/m^{2}s, $P_n = 1.5 - 2.5\ bar$	-	1.05 ≤ U[1]≤ 9.06	(C8)
Hsieh et al. (2004) [32]	**R-134a**	$\Delta T_{sub} = 2 - 4\,^{\circ}C$, $We = 50 - 152$, $H = 60mm$, $d_{32} = 42 - 46\ \mu m$, $G = 0.064 - 0.108$ kg/m^{2}s, $P_n = 6.2 - 7.2\ bar$	-	1.05 ≤ U ≤ 9.06	(C9)
Ghodbane and Holman (1990) [33]	**R-134a**	$d_{05} = 210 - 980\ \mu m$, $u_m = 5.4 - 28\ m/s$, $q = 0.001 - 0.5\ MW/m^2$, $T_c = 5 - 10^{\circ}C$, $H = 18 - 35cm$, $We = 2200 - 13750$	-	-	(C10)
Rybicki and Mudawar (2006) [34]	**water** **PF-5052**	$\Delta T_{sub} = 76 - 77\,^{\circ}C$, $d_{32} = 109 - 151\ \mu m$, $\bar{\dot{v}} = 35 - 186$ m^{3}s^{-1}/m^2 $\Delta T_{sub} = 23 - 27\,^{\circ}C$, $d_{32} = 109 - 151\ \mu m$, $\bar{\dot{v}} = 35 - 186$ m^{3}s^{-1}/m^2	MAE[2]=22.7	-	(C11)
Pereira et al. (2013) [35]	**water**	4-5 array of full cone nozzles: $\Delta T_{sub} = 30 - 75\,^{\circ}C$, $G = 0.3 - 7.2$ kg/m^{2}s	MAE=10.6	1.3 ≤ U ≤ 1.7	(C12)
Dou et al. (2015) [36]	**water**	$T_c = 15 \pm 1^{\circ}C$, $P_n = 2 - 5\ bar$, $v = 30 - 50\ l/min$	±25	ARE[3]=6.3	(C13)
Qiao and Chandra (1998) [35]	**water additive**[4]	$G = 2.8$ kg/m^{2}s, $P_n = 1.38 - 2.76\ bar$, $u_m = 17 - 23$ m/s	-	-	(C14)
Mudawar and Valentine (1989) [38]	**water**	$T_c = 23 \pm 0.5^{\circ}C$, $\bar{\dot{v}} = 0.06 - 9.96$ m^{3}s^{-1}/m^2, $u_m = 10.6 - 26.7$ m/s $d_{05} = 434 - 2005\ \mu m$	-	-	(C15)

[1]Uncertainty, [2]Mean absolute error, [3]Average relative error, [4]100-ppm sodium dodecyl sulfate

Table 1. Continued:

*Developed correlations associated with Refs. [18][20 -33] identified by Equations C1 to C15 as appropriate:

$$Bo_m = c(We)^m(Ja)^n(H/L)^r,\ c = 12.3,\ m = 0.525,\ n = 1.854, \text{ and } r = 0.924. \quad \text{(C1)}$$

$$Nu = 1.031\left[\bar{\vec{v}}\delta\left(\frac{C_l\mu_l}{k_l}\right)^{0.5}\frac{\rho_l g^{0.25}}{h_{fg}\sigma^{0.75}\rho_v^{1.25}}\right]^{0.655} \quad \text{(C2)}$$

$$q = 0.245\rho_l h_{fg}u_d\left[\frac{C_l\Delta T_{sat}}{h_{fg}}\right]^{1.038}\left[\frac{\rho_l\sigma\dot{m}}{\mu_l{}^3}\right]^{0.133}\left[\frac{\Delta T_{sat}}{\Delta T_{sub}}\right]^{-0.491}\left[\frac{R_t}{d_d}\right]^{0.0213}\left[\frac{P_{am}}{P_{at}}\right]^{0.291} \quad \text{(C3)}$$

$$q = 1.7453\rho_l h_{fg}\bar{\vec{v}}\left[\frac{C_l\Delta T_{sat}}{h_{fg}}\right]^{1.5286}\left[\frac{\rho_l u_m{}^2 d_{32}}{\sigma}\right]^{-0.3514}\left[\frac{\rho_l\sigma\dot{m}}{\mu_l{}^3}\right]^{0.1643}\left[\frac{\Delta T_{sat}}{\Delta T_{sub}}\right]^{-0.1946} \quad \text{(C4)}$$

$$q = 120Q[1 + 0.25(\cos\alpha)^{1.75}]\left[\frac{\Delta T_{sat}}{\Delta T_{sub}}\right]^{0.3} \quad \text{(C5)}$$

$$q = 133v\left[\frac{\Delta T_{sat}}{\Delta T_{sub}}\right]^{0.47} \quad \text{(C6)}$$

$$q = 9.4\frac{k_l h_{fg}}{d_H C_l}\left[\frac{C_l\Delta T_c}{h_{fg}}\right]^{1.12}\left[\frac{\rho_l u_m d_H}{\mu_l}\right]^{0.3}\left[\frac{u_m}{\bar{\vec{v}}}\right]^{0.16}\left[\frac{d_H}{d_{32}}\right]^{0.24} \quad \text{(C7)}$$

$$q = 33.595\frac{\mu_l h_{fg}}{H}\left[\frac{C_l\Delta T_c}{h_{fg}}\right]^{1.68}\left[\rho_l\left(\frac{2\Delta P}{\rho_l}\right)d_n\left(\frac{\rho_v^{0.5}\Delta P d_n^{1.75}}{\sigma^{0.5}\mu_l}\right)^{-0.259}/\sigma\right]^{0.59} \quad \text{(C8)}$$

$$Bo_m = C(We)^m(Ja)^n,\ c = 2.1,\ m = 0.66,\ n = 1.51 \quad \text{(C9)}$$

$$q = 10.55\frac{\mu_l h_{fg}}{H}\left[\frac{C_l\Delta T_c}{h_{fg}}\right]^{1.46}\left[\frac{\rho_l u_m^2 d_{0.5}}{\sigma}\right]^{0.6} \quad \text{(C10)}$$

$$q = 4.79\times10^{-3}\frac{\mu_l h_{fg}}{d_{32}}\left[\frac{C_l\Delta T_c}{h_{fg}}\right]^{5.75}\left[\frac{\rho_l\bar{\vec{v}}^2 d_{32}}{\sigma}\right]^{0.35}\left[\frac{\rho_l}{\rho_v}\right]^{2.5} \quad \text{(C11)}$$

$$q = 2067(T_w - T_{sat})^{1.57} \quad \text{(C12)}$$

$$q = 1.837\times10^4(T_w - T_c)^{0.69} \quad \text{(C13)}$$

$$q = 0.56\times10^{-5}(T_w - T_c)^6 \quad \text{(C14)}$$

$$q = 1.87\times10^{-5}(T_w - T_c)^{5.55} \quad \text{(C15)}$$

2 Experimental measurement facilities

Figure 3a and Figure 3b show the test-piece located in a chamber, attached by a shaft to a mechanical shaker (Bruel & Kjaer V555). The test piece and nozzle inside the chamber can be simultaneously shaken at different amplitudes and frequencies. The amplitude and frequency of the shaker was controlled using a Feedback Instruments FG600 signal generator with a pure sine wave option. A Piezotronics PCB A 353B15 accelerometer (10.27 mV/g, 1 Hz - 10 kHz) is attached to the bottom of the drive shaft bolted to the shaker head. Corresponding acceleration signals were measured by a National Instruments data acquisition system. The test piece is a copper disc with a diameter of 20 mm, with a smooth surface and a thermal conductivity of 385 Wm/K. Three T-Type thermocouples are used, the first of which is located 1 mm under the coolant surface of the test chamber, followed by two more thermocouples evenly located 5.5 mm below each other. This is to facilitate heat flux measurement capabilities. The test piece is heated by six Watlow 250W cartridge heaters controlled by 0 to 5 V signals from an NI9264 module and a power regulator (EVR-25BF). Figure 3c shows a cross-sectional CAD view of the chamber, including the test piece, heater block, shaker, bolts and a shroud. There is an 88 mm clearance between the cylindrical wall of the chamber

and the edge of the test piece surface. This clearance is made possible by the choice of dimensions of the chamber (a cylinder with an internal diameter of 196 mm, and the 20 mm disc test-piece). The 88 mm clearance adequately minimizes the risk of droplet reflection (from the surrounding walls) onto the spray flow field. Changes to the nozzle-to-surface arrangement (plus knowledge of the spray characteristics for different operating conditions) enables the spray covering diameter to range from 16 mm to 25 mm. This ensures that the spray impinges only onto the test piece and the shroud. The characteristics of the spray available from a UNIJET® HYDRAULIC SPRAY- TG tip-type nozzle used, are summarised from manufacture's data and given in Table 2.

Table 2. Spray specification for the operating conditions of the UNIJET **nozzle.**

UNIJET TG HYDRAULIC FULL CONE SPRAY SPECIFICATION						
d_n (mm)	α (◦)	Covering d. (mm)	$\Delta P\ (bar)$	$u_m(\frac{m}{s})$	d_{05} (µm)	d_{32} (µm)
0.51	50 - 61	16 - 25	1.3 - 3	16.5 - 25	89 - 146	198 - 246

Figure 4 shows a schematic view of the complete experimental test system and test rig which comprises the following components. Firstly, a pump (Micropumps MGD100P) supplies de-ionised water to the full-cone UNIJET® nozzle (TG tip-type, ranging from 0.14 litres/min at 1.3 bar, to 0.39 litres/min at 10 bar). The nozzle is located on top of the test chamber. Second, a tank separates vapour and liquid and delivers it to the condenser and condensate tank. Third, an air-cooled condenser (Denso RDP 583) where vapour from the test chamber is vented through a throttle valve. A miniature heat exchanger cools the condensate (at exit from the condenser) to below the maximum operating temperature of the pump (100 ˚C). Two 345 W band-heaters (see the feed heater in Figure 4) with a controllable 0 to 5 V power regulator (United Automation, EVR-25BF, AC Burst Fire Controller) heat the feed-water to the nozzle to obtain different degrees of sub-cooling (i.e. the difference between saturation and inlet temperatures). The feedwater temperature is regulated by a PID controller in the CRIO-9035 National Instrument. Two digital pressure transducers (Omega PXM309) are linked to the data acquisition system to provide a constant record of the chamber pressure and the nozzle pressure difference. A low-flow turbine meter (Omega FLR1009ST-D) is situated just after the pump to measure the flow-rate, and is used as a state variable for the PID controller in FPGA CRIO-9035 to control the pumping voltage. This enables constant flow rates to be obtained during experimentation. A header tank is also fitted at the highest point in the circuit to remove air and provide a positive feed.

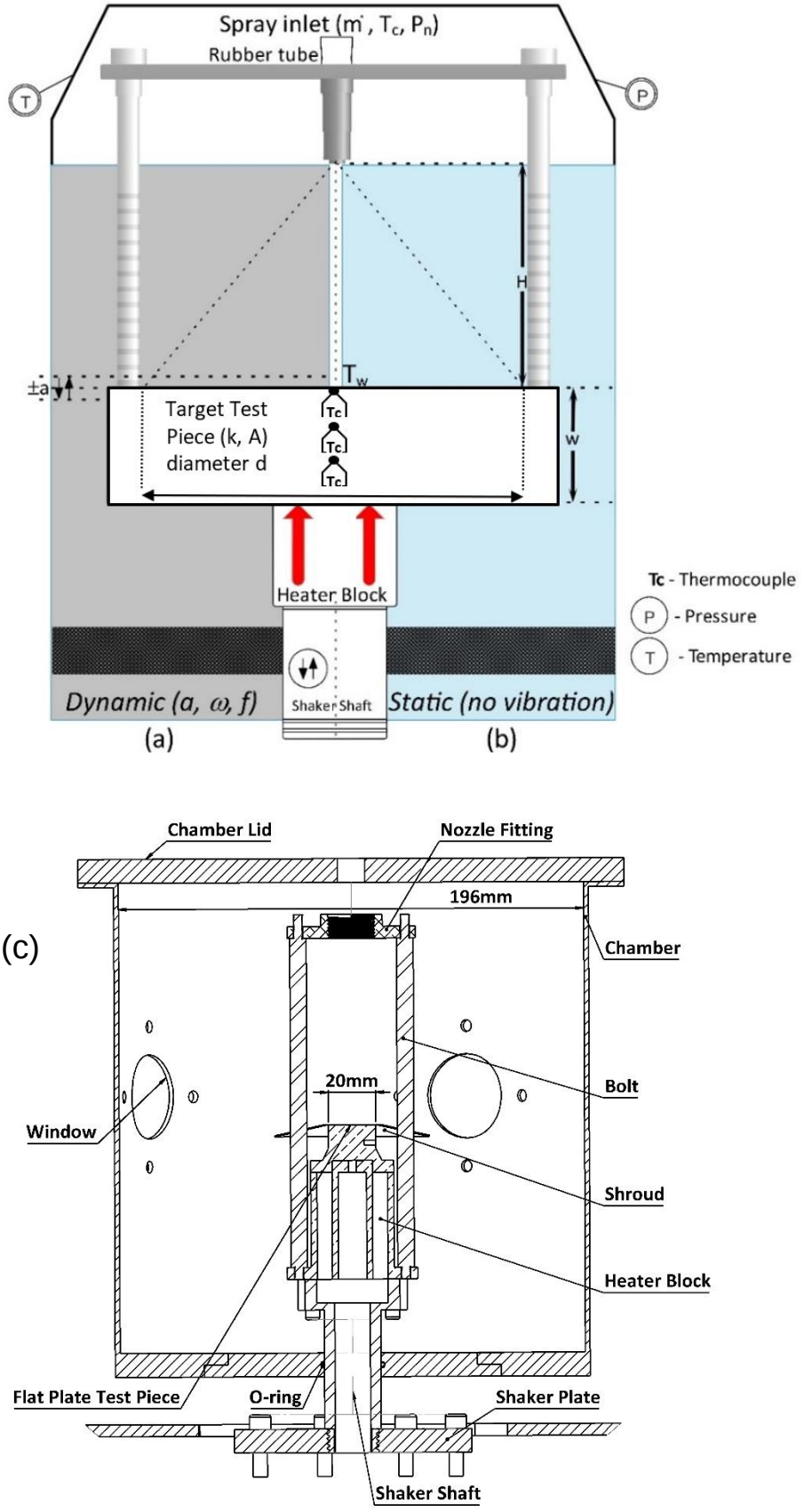

Fig. 3. Spray system configuration inside the chamber under: a) dynamic, and b) static conditions (not to scale); and c) Cross-sectional CAD view to scale, taken from [56].

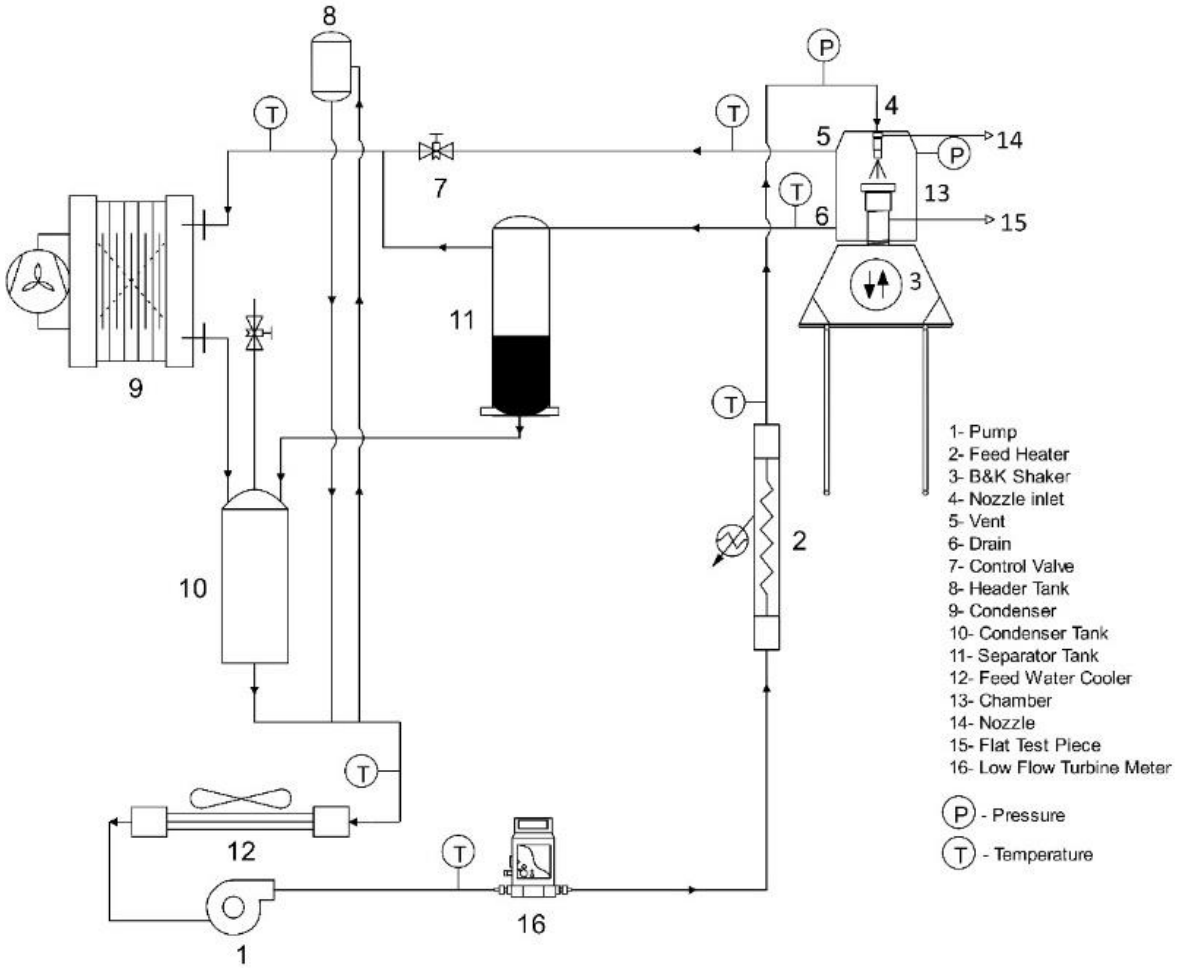

Fig. 4. Schematic view of the complete experimental test system and test rig

3 Dimensional analysis and the Generalized Π –Theorem

Dimensional analysis is one of the most important steps in pre-experimental planning and modelling phases [39]. Implementing dimensional analysis such as via the Buckingham Π-Theorem [40,41], and developing from it, only important dimensionless parameters, reduces the amount of data measurement required, and significantly reducing resource needs. Initiating dimensional analysis before quantitative analysis also helps reach an understanding of a problem with minimum complexity, which is highly beneficial when investigating novel phenomena, for which the governing equations of a model and associated boundary conditions are not yet fully established [42].

In constructing a model for heat flux, dimensional analysis must be based on a complete set of independent parameters. Preliminary investigation shows that some independent variables exist which also define the dependent variable of interest. These should have invariant values in all cases under consideration. For example, in spray cooling, all sets of experimental measurements should be taken at the same chamber pressure, and in equilibrium conditions. However, in two-phase flow, some of the fluid properties (which act as independent variables) define the heat flux (a dependent variable) and have the same invariant values. This is also true of the spray specifications in experimental measurements using the same nozzle. Neglecting quantities which have the same value, can however adversely affect the dimensional analysis. To avoid this difficulty, the

Generalized Π-Theorem [43] is used from now on to establish the appropriate forms of correlation model, first without, and then with, cooling surface vibration.

Based on the experimental test rig available (as shown in Figure 3 and Figure 4), measurements can be obtained either with or without mechanically-induced vibration. The use of a National Instruments data acquisition (DAQ) system allows data to be collected corresponding to different system states. For static measurements during nucleate boiling (as summarised by Table 1), heat flux, as a dependent variable, can be fully determined from the fluid properties, geometry, forcing, and spray specifications as provided in the functional relationship demonstrated by the following function:

$$q = \varphi(\rho_l, \rho_v, h_{fg}, \mu_l, C_l, \sigma, T_c, T_w, P_n, P_{ch}, \Delta T_c, \Delta T_{sat}, \Delta T_{sub}, P_{at}, u_d \text{ or } u_m, \dot{m}, d_{32}, d_H, H) \quad (1)$$

where in Equation (1), the variables $\dot{m}$ and d_{32} can be replaced by v, or d_{05} respectively. All quantities are described in Table 3 (which gives the units in both SI and MLT systems). It should be noted that all key parameters in equation (1) are used in different empirical correlations of spray cooling. These are available in Table 1 and are discussed in [6].

There are currently no studies in the literature that have employed dimensional analysis for dynamic measurements (i.e. in the presence of vibration). Therefore, no correlation has yet been developed to predict the heat flux in nucleate boiling under dynamic conditions. There is however a study on two-phase flow spray characteristics including vibration. This is a purely numerical investigation which uses the *Volume of Fluid* (VOF) method [44] on the effect of single and multiple droplets on a vibrating surface. In order to develop a relation for the first time, basic fluid dynamics suggests that heat flux should at least be based on those independent parameters appropriate for static conditions. It should also use vibration amplitude a, vibration frequency $\omega = 2\pi f$, and to characterise acceleration, the gravitational constant g. Therefore, the proposed functional form for nucleate boiling is as follows:

$$q = \varphi(\rho_l, \rho_v, h_{fg}, \mu_l, C_l, \sigma, T_c, T_w, P_n, P_{ch}, \Delta T_{sat}, \Delta T_{sub}, P_{at}, u_d \text{ or } u_m, \dot{m}, d_{32}, d_H, H, a, \omega, g) \quad (2)$$

where also in Equation (2) the variables $\dot{m}$ and d_{32} can be replaced by v, or d_{05} respectively. The dimensions, and a description of different parameters, are given in the Table 3.

Table 3. Parameters with dimensions in SI and MLT systems.

		Dimensions	
Quantity	Symbol	SI	MLT
q	Heat Flux	kW/m^2	MT^{-3}
ρ	Density	kg/m^3	ML^{-3}
h_{fg}	Latent heat	kJ/kg	L^{2}T^{-2}
μ	dynamic viscosity	Kg/m s	ML^{-1}T^{-1}
C_l	specific heat	kJ/kg k	L^{2}T^{-2}θ^{-1}
σ	surface tension	N/m	MT^{-2}
P	pressure	kPa	ML^{-1}T^{-2}
T	temperature	K	θ
u	velocity	m/s	LT^{-1}
$\dot{m}$	Mass flow rate	kg/s	MT^{-1}
v	Volumetric flow rate	m^3/s	L^3 T^{-1}
$\bar{\vec{v}}$	Average volumetric spray flux, $\bar{\vec{v}} = \frac{v}{\pi(Htan(\frac{\alpha}{2}))^2}$, α is spray angle	m^{3}s^{-1}/m^2	LT^{-1}
d_{32}	Sauter mean diameter	m	L
d_{05}	mass or volume median diameter	m	L
d_H	Hydraulic diameter of the heating surface	m	L
H	Height from nozzle to surface	m	L
a	Amplitude	m	L
ω	Angular frequency	1/s	T^{-1}
g	Acceleration of gravity	m/s^2	LT^{-2}

After defining independent variables (key parameters) Dimensional Analysis is undertaken. To determine the number of Π-terms in the procedure [43], invariant parameters in different case studies need to be identified. Invariant parameters (e.g. Chamber Pressure) can be identified according to the test plan. For example, experiments are only conducted under atmospheric pressure. Following Dimensional Analysis, the dimensionless Π-parameters (which entirely comprise invariant quantities, with fixed values) can be omitted, resulting in further simplification. As a result of applying this form of Dimensional Analysis, all the derived functional forms corresponding to different spray evaporative cooling with test plans for both dynamic and static conditions are provided in Table 4 (i.e. for Nucleate boiling; Equations (1) and (2)).

Table 4. Functional forms of spray cooling heat flux in nucleate boiling regime

Environment	Invariant Parameter	Number of Π-terms	Measure--ments needed	Functional form
Static (No vibration)	None	5	Spray spec.[3]	$\frac{qH}{\mu_l h_{fg}} = f\left(\frac{C_l\Delta T}{h_{fg}}, \frac{\rho_l(u_m^2 or \bar{\vec{v}}^2)d_{32}}{\sigma}, \frac{\Delta T_{sat}}{\Delta T_{sub}}, \frac{P_{ch}}{P_{at}}, \frac{\rho_l}{\rho_v}\right)$
			flow rate	$\frac{qH}{\mu_l h_{fg}} = f\left(\frac{C_l\Delta T}{h_{fg}}, \frac{\rho_l\sigma\dot{m}}{{\mu_l}^3} or \frac{{\rho_l}^2\sigma v}{{\mu_l}^3}, \frac{\Delta T_{sat}}{\Delta T_{sub}}, \frac{P_{ch}}{P_{at}}, \frac{\rho_l}{\rho_v}\right)$
	P_{ch}[1]	3	Spray spec.	$\frac{qH}{\mu_l h_{fg}} = f\left(\frac{C_l\Delta T}{h_{fg}}, \frac{\rho_l(u_m^2 or \bar{\vec{v}}^2)d_{32}}{\sigma}, \frac{\Delta T_{sat}}{\Delta T_{sub}}\right)$
			flow rate	$\frac{qH}{\mu_l h_{fg}} = f\left(\frac{C_l\Delta T}{h_{fg}}, \frac{\rho_l\sigma\dot{m}}{{\mu_l}^3} or \frac{{\rho_l}^2\sigma v}{{\mu_l}^3}, \frac{\Delta T_{sat}}{\Delta T_{sub}}\right)$
	P_{ch}, ΔT_{sub}[2]	2	Spray spec.	$\frac{qH}{\mu_l h_{fg}} = f\left(\frac{C_l\Delta T}{h_{fg}}, \frac{\rho_l(u_m^2 or \bar{\vec{v}}^2)d_{32}}{\sigma}\right)$
			flow rate	$\frac{qH}{\mu_l h_{fg}} = f\left(\frac{C_l\Delta T}{h_{fg}}, \frac{\rho_l\sigma\dot{m}}{{\mu_l}^3} or \frac{{\rho_l}^2\sigma v}{{\mu_l}^3}\right)$
Dynamic	*None*	8	Spray spec.	$\frac{qH}{\mu_l h_{fg}} = f\left(\frac{C_l\Delta T}{h_{fg}}, \frac{\rho_l(u_m^2 or \bar{\vec{v}}^2)d_{32}}{\sigma}, \frac{\Delta T_{sat}}{\Delta T_{sub}}, \frac{P_{ch}}{P_{at}}, \frac{\rho_l}{\rho_v}, \frac{a}{H}, \frac{\omega^2 a}{g}, \frac{\omega a}{u_d}\right)$
			flow rate	$\frac{qH}{\mu_l h_{fg}} = f\left(\frac{C_l\Delta T}{h_{fg}}, \frac{\rho_l\sigma\dot{m}}{{\mu_l}^3}, \frac{\rho_l a\omega d_H}{\mu_l}, \frac{\Delta T_{sat}}{\Delta T_{sub}}, \frac{P_{ch}}{P_{at}}, \frac{\rho_l}{\rho_v}, \frac{a}{H}, \frac{\omega^2 a}{g}\right)$
	P_{ch}	6	Spray spec.	$\frac{qH}{\mu_l h_{fg}} = f\left(\frac{C_l\Delta T}{h_{fg}}, \frac{\rho_l(u_m^2 or \bar{\vec{v}}^2)d_{32}}{\sigma}, \frac{\Delta T_{sat}}{\Delta T_{sub}}, \frac{a}{H}, \frac{\omega^2 a}{g}, \frac{\omega a}{u_d}\right)$
			flow rate	$\frac{qH}{\mu_l h_{fg}} = f\left(\frac{C_l\Delta T}{h_{fg}}, \frac{\rho_l\sigma\dot{m}}{{\mu_l}^3} or \frac{{\rho_l}^2\sigma v}{{\mu_l}^3}, \frac{\rho_l a\omega d_H}{\mu_l}, \frac{\Delta T_{sat}}{\Delta T_{sub}}, \frac{a}{H}, \frac{\omega^2 a}{g}\right)$
	P_{ch}, ΔT_{sub}	5	Spray spec.	$\frac{qH}{\mu_l h_{fg}} = f\left(\frac{C_l\Delta T}{h_{fg}}, \frac{\rho_l(u_m^2 or\ \bar{\vec{v}}^2)d_{32}}{\sigma}, \frac{a}{H}, \frac{\omega^2 a}{g}, \frac{\omega a}{u_d}\right)$
			flow rate	$\frac{qH}{\mu_l h_{fg}} = f\left(\frac{C_l\Delta T}{h_{fg}}, \frac{\rho_l\sigma\dot{m}}{{\mu_l}^3} or \frac{{\rho_l}^2\sigma v}{{\mu_l}^3}, \frac{\rho_l a\omega d_H}{\mu_l}, \frac{a}{H}, \frac{\omega^2 a}{g}\right)$

[1]Constant pressure, [2]Constant pressure and degree of subcooling, [3]Spray specifications

Based on the test rig capability, three different test plans are considered for experiments in static and dynamic environments. The first plan uses variable pressure and the degree of subcooling (i.e. '*None'* invariant parameter in Table 4). The second plan uses constant pressure (with invariant P_{ch} in the second column of Table 4). The third plan uses constant pressure and the degree of subcooling (P_{ch}, ΔT_{sub}). To undertake experiments with constant pressure (above atmospheric only) the test rig is equipped with a control valve (See Figure 4), which can be adjusted manually if required. In order to control the degree of subcooling ($\Delta T_{sub} = T_{sat} - T_c$), the saturation temperature T_{sat} can be held at a constant value by the same control valve which keeps chamber pressure constant. This is a result of the equilibrium nature of two-phase flow. A temperature PID controller can be used to set the inlet temperature T_c at a constant value by actuating the feed-heater load (i.e. Number 2 on Figure 4). And as is provided in the third column of Table4, the number of Π-terms are reduced for the functional forms obtained, from '*None'* invariant parameters to those for fixed P_{ch} and ΔT_{sub}, a result of the Generalized Π–Theorem algorithm.

Furthermore, dimensionless functional forms can be derived based on modelling requirements and expectations; designated here by: *spray specifications* and *flow rate* (i.e. the fourth column of Table 4). Whether, for instance, it is for a design purpose in which spray specifications are important, or a special control approach that the pumping flow rate (either $\dot{m}$ or v) plays an important role on the wall temperature control, different dimensionless Π–terms can be obtained as shown in the last column of Table 4. In other words, these Π–terms can simplify measurement requirements, such as *spray specifications* which are usually costly and time consuming to obtain. They also make system identification easier.

Table 4 shows three dimensionless numbers which are well known in fluid mechanics. These are the Boiling Number ($Bo = qH/\mu_l h_{fg}$), the Jacob Number ($Ja = C_l \Delta T/h_{fg}$), and the Weber Number $We = \rho_l(u_m^2 or\, \overline{v}^2)d_{32}/\sigma$. In the functional forms corresponding to '*flow rate*' measurements, another Π–term is substituted for Weber Number. This Π–term is: '$\rho_l \sigma \dot{m}/{\mu_l}^3$ or ${\rho_l}^2 \sigma v/{\mu_l}^3$', which contains mass ($\dot{m}$) or volumetric flow rate (v) instead of spray specifications of '$u_m\ or\ \overline{v}$' and 'd_{32}' in the Weber Number. What is interesting about the functional forms associated with the dynamic condition is that a Vibrational Reynolds Number $Re_V = \rho_l a \omega d_H/\mu_l$ is obtained. In fact, Vibrational Reynolds Number is a representation of the turbulence resulting from the vibrating surface [24]. It is a metric to understand how vibration through the enhanced turbulence can affect heat transfer. Hypothetically, heat transfer enhancement or attenuation, as a consequence of the vibration field (if there is any) can be explained by increased flow turbulence, a thinned or thickened boundary layer, more or less generated nucleate sites [45] and the changed wetting-angle [44]. In addition, there is a dimensionless acceleration number, $\omega^2 a/g$ in the dynamic functional forms. The dimensionless acceleration number is helpful in considering any possible effect of experimentally-measured acceleration (using an accelerometer). The effect of acceleration on the spray cooling heat transfer has been empirically investigated in the following dynamic conditions: An acceleration test bench with a rotating arm [46], a reduced gravity condition [47], and on an aircraft doing parabolic flights [48, 49]. However, there are inconsistencies in the conclusions, owing to the complexity of spray heat transfer mechanisms and differences in experimental conditions. Thus, acceleration stemmed from the vibrational environment (which is different to aerospace conditions in terms of heater orientation), is also of importance to the understanding of spray cooling for all dynamic conditions such as for automotive and aerospace vehicle applications.

4 Experimental test procedure and data reduction

A total of 70 sets of experiments were undertaken for both *static* conditions (without vibration) and *dynamic* conditions (with vibration at frequencies ranging from 1.9 to 400 Hz). The vibration test amplitude ranges from ± 0.02 to ± 12 mm. Table 5 gives the test data for this empirical study.

Table 5. Test plan and operating parameters.

$P_{chamber}$ (bar)	v (ml/min)	$T_{coolant}$ (°C)	H (mm)	Static	f(Hz) / a (mm)	1.9	3	6	10	60	100	200	400
1	140, 160, 180 and 200	Constant at 80±1.5°C	17 and 21	✓	0.02	-	-	-	-	-	✓	✓	✓
					0.1	-	-	-	✓	-	✓	-	-
					0.08	-	-	-	-	-	-	✓	-
					0.2	-	-	-	-	✓	-	-	-
					1	-	-	-	✓	✓	-	-	-
					2	-	✓	✓	-	-	-	-	-
					4	-	✓	✓	-	-	-	-	-
					8	-	✓	✓	-	-	-	-	-
					12	✓	-	-	-	-	-	-	-

During each test-run, the data for any new state was collected between 3 to 7 minutes (depending on the thermal inertia) after changing the cartridge heater loads to make sure that the system reached the steady state conditions. A test-run for the case study involving *static* cooling surfaces with a flow rate of $180\ \mathrm{ml/min}$ was conducted twice for the purposes of checking repeatability of the test facility. The heat flux was calculated using a solution for the one-dimensional conduction equation:

$$q = -k\frac{dT}{dx} \tag{3}$$

Using measurements taken from thermocouples embedded in the test piece, where k, dT, and dx are the thermal conductivity, the temperature difference, and the distance between the top and bottom thermocouples located in the test piece i.e. 11 mm.

4.1 Uncertainty analysis

To describe the uncertainties in the current experimental study, a method by Moffat [50] was utilised as follows:

$$\delta R = \left[\sum_{i=1}^{n}\left(\frac{\partial R}{\partial X_i}\delta X_i\right)^2\right]^{\frac{1}{2}} \tag{4}$$

where δR is the uncertainty of the dependent parameter is equal to the root square sum of sensitivity coefficient ($\frac{\partial R}{\partial X_i}$) multiplied by the error in the measurement (δX_i). For the heat flux, the uncertainty can be calculated from the following equation:

$$\delta R_q = \left[\left(\frac{k}{dx}\delta dT\right)^2 + \left(\frac{-kdT}{dx^2}\delta dx\right)^2\right]^{1/2} \tag{5}$$

where the maximum uncertainty in the calculation of heat flux, at the maximum experimentally-measured data point of 3.23 MW/m^2 is expected to be 2.97%. Table 6 gives the measurement errors and parameter uncertainties.

Table 6. Uncertainties of the measured and calculated quantities.

Parameter	Uncertainty (%)	Units
Thermocouples	±0.4	℃
Pressure transducers	±0.25	bar
Volumetric flow rate	±0.6 (of full scale)	ml/min
Diameter	±1	mm
Length	±1	mm
Accelerometer amplitude	±10	mm
Accelerometer frequency	±5	Hz
Heat flux	±2.97	MW/m^2

5 Results and discussion

This section provides the results of the static and dynamic case studies, as well as the developed correlations. First there is a comparison between the equivalent boiling curves (with and without mechanically-induced vibration) to assess the prospective influence of vibration on the heat flux. Next there is a discussion of the effects of low to high frequencies as well as small to large amplitudes to further understand the trend of vibration over static results. The final section presents the results of the fitted data to the relevant correlations (already derived by Dimensional Analysis). There is also a discussion of prediction error bands, which play a vital role in the development of a concise and reliable model for spray cooling under static and dynamic conditions.

5.1 Static surface results

Figure 5 shows the effects of volumetric flow rate and nozzle-to-surface distance on the measured heat flux over different excess temperatures. The excess temperature ΔT is defined as the difference between the sprayed surface temperature and the coolant saturation temperature (i.e. $\Delta T = T_s - T_{sat}$). Two different nozzle-to-surface distances are 17 and 21 mm. The volumetric flow rate ranges from 140 and 200 $\mathrm{ml/min}$, the heat flux ranges from 360 $\mathrm{kW/m^2}$ to 3070 $\mathrm{kW/m^2}$ and the excess temperature ranges from 9.5 to 70 ˚C. An increase in the flow rate at most of the equivalent excess temperatures gives rise to an increase in heat flux. However, there are two important reverse trends. One occurred when the flow rate is increased from 160 to 180 $\mathrm{ml/min}$ for the nozzle height of 21 mm, there is actually a slight reduction in the heat flux during all excess temperatures rather than an increase. The second occurred at an excess temperature of around 10 ˚C where there is a reverse trend in the heat flux result for the flow rate of 140 $\mathrm{ml/min}$, which has a slightly greater value than those for 160 and 180 $\mathrm{ml/min}$.

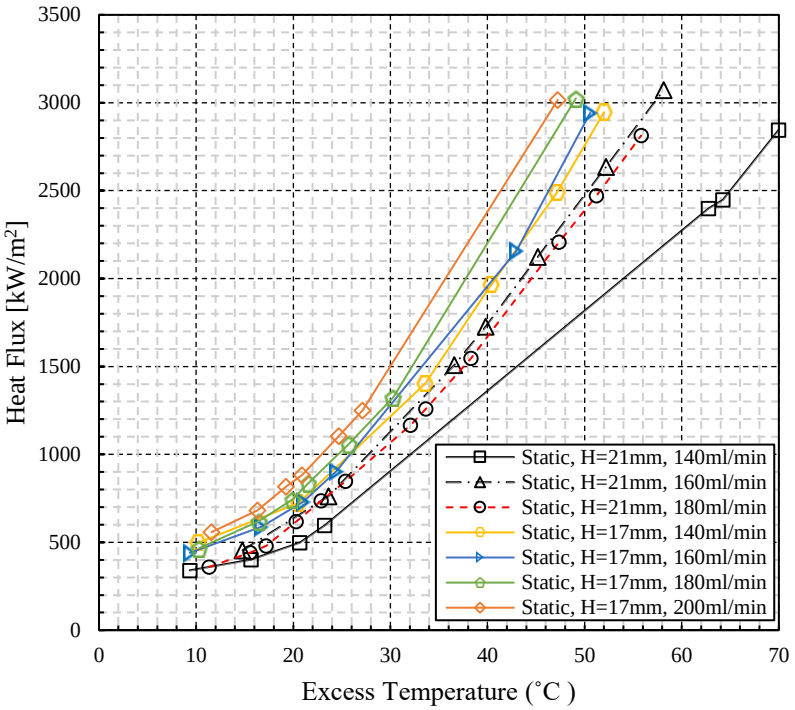

Fig. 5. Nucleate boiling curves for the case study involving static cooling surfaces.

It can be hypothesised that the first reverse trend is a result of an increased spray angle. In this case, a higher volumetric flow rate causes a higher pressure difference across the nozzle, i.e. here, from 1.6 bar to 2.3 bar. It is stated on the (UNIJET® nozzle, TG tip Type) manufacturers data sheet, that the spray angle varies from 50˚ to 61˚. This hypothesis is supported by two studies. In their research about the effect of spray angle on spray cooling performance, Schwarzkopf et al. [51] reports a heat transfer attenuation when the spray angle exceeds 50˚. In this case, increased spray cone-angle at 180 ml/min means lower effective volumetric flow rate covering the test piece, providing less heat-transfer compared to that for a lower volumetric flow rate of 160 ml/min but with a higher effective flow rate. The same reverse trend has been observed by Zhang et al [46]. In support of this observation, readers should refer to the results for the smaller nozzle-to-surface distance of 17 mm for 160 and 180 $\mathrm{ml/min}$ in Figure 5. Thus, with an increase in flow rate, the spray is able to increase its mass flow rate per unit area. In general, the trend shows that the effect of reducing the surface-to-nozzle distance is beneficial to the heat transfer and therefore increases the heat flux during all of the excess temperature regions. It is possible to maintain the same volumetric flux even with a reduction in cone angle by reducing the height H. This is evident from the volumetric flux equation [52]:

$$\bar{\vec{v}} = \frac{v}{\pi(Htan\left(\frac{\alpha}{2}\right))^2} \tag{6}$$

where $\bar{\vec{v}}$ is the volumetric flux, v is volumetric flow rate, α represents spray cone angle, and H is nozzle-to-surface distance. Owing to the limited experimental conditions, it was impossible to find a precise threshold for the reduced volumetric flux caused by the cone angle alteration.

Furthermore, a reduction in the nozzle-to-surface distance results in an increased momentum, droplet impact velocity, and more droplet-liquid film interactions, which can also lead to the heat transfer enhancement [53]. The droplet impact velocity or droplet breakup velocity can be obtained from a simple energy balance analysis developed by Ghodbane and Holman [33]. It is then developed by Qiao and Chandra [54] in a way to include gravitational potential energy and formulated as follows:

$$u_m = \left(u_o^2 + \frac{2\Delta P}{\rho_l} - \frac{12\sigma}{\rho d_{05}} - 2gHsin(\alpha)\right) \tag{7}$$

where u_o, ΔP and d_{05} are respectively the mean velocity of water entering nozzle, the pressure drop across spray nozzle, and the mass median droplet diameter.

The second reverse trend (at an excess temperature of 10 ˚C) can be explained by a smaller droplet impact velocity onto the thin layer of water accumulated on the surface for the data point at $140\ \mathrm{ml/min}$, owing to a lower pressure difference around the nozzle (here 1.3 bar for $140\ \mathrm{ml/min}$ comparing to 1.6 and 2.3 bar for 160 and 180 $\mathrm{ml/min}$). Such an incident makes a lower penetration effect lead to the advent of nucleation at a lower surface temperature, owing to less suppression force in front of bubble departure from nucleation sites. The conclusion is that leading the advent of the nucleate boiling regime to a lower surface temperature enhances the heat transfer coefficient at the same excess temperature.

The flow rate and nozzle specification are chosen to typically correspond to the cooling system of a hybrid electric vehicle. These requirements are adopted to address identified thermal management problems [1] such as controlling steady-state surface temperature with heat flux levels in the range 0 - 2 MW/m^2. These thermal requirements are feasible in the nucleate boiling regime [2] which is a primary motivation of generating appropriate experimental data. However, the operating conditions and parameters are limited by the pump power (using a Micropumps MGD100P model) which is not capable of providing a higher flow rate with the chosen nozzle. This MGD100P pump was chosen to provide a Coefficients of Performance of between 1 - 4 (i.e. the ratio: Heat Flux/Pump Electrical Power) which is the typical situation arising when cooling high-powered electrical systems found in hybrid and battery-powered vehicle cooling systems. Moreover (according to the manufacturer's datasheet), the UNIJET® nozzle does not have a full cone spray for flow rates lower than the prevailing operating region (i.e. 140 ml/min). Our experimental findings are therefore restricted to the stated operating conditions and parameters. Extending the operating conditions could therefore conceivably change the overall trend.

The measurements presented shortly focus solely on the nucleate boiling regime of evaporative spray cooling. Excursions into the critical heat flux (CHF), and beyond into the transition boiling regime, were experienced in the commissioning phase of the experimental test facilities. It is well known however that once the CHF is reached, the subsequent transition boiling regime is unstable. As a result of a vapour film replacing the liquid film adjacent to the surface, the heat flux decreases, and the surface temperature increases. This phenomenon was, as previously mentioned, observed in the commissioning phase. The rise in surface temperature is very rapid occurring within seconds and exceeds 300°C. This was considered to pose a danger to the experimental test rig, in particular to the cartridge heaters which have a maximum operating temperature of 450°C.

5.2 Dynamic surface results

Firstly, the influence of vibration on the heat transfer will be investigated in the middle range operating conditions. Then, the results of harsh dynamic conditions, including high frequency vibration with small amplitudes, and large amplitude vibration at low frequencies, will be thoroughly evaluated to cover a wide operating condition. In addition, the results associated with the effect of flow rate and nozzle-to-surface distance are compared for high frequency vibration and the relationship between them has been explained (i.e. for two nozzle heights). This is because the trend showing the effect of vibration for different flow rates and nozzle heights may be different. (In particular having the information in the same figure provides an opportunity to study the influences of flow rate and nozzle height in the presence of vibration). Large amplitude results represent typical dynamic operating conditions associated with real vehicle dynamics, a primary focus of the study.

5.2.1 The effect of varying flow rate on heat flux with and without surface vibration

Figure 6, Figure 7, and Figure 8 show the heat flux as a function of excess temperature for the test results with flow rates between 140 $\mathrm{ml/min}$ and 180 $\mathrm{ml/min}$ at nozzle height of 21 mm in middle frequency range vibrations. Also shown on each figure (and later figures) is the *effect ratio*. This is defined as the ratio of the dynamic-heat-flux/static-heat-flux which in all cases (except for Figure 6c) uses the dynamic case that produces the largest effect. First, to inspect the *static* and *dynamic* results for any influence of amplitude on the heat flux, two fixed frequencies of 10 Hz and 60 Hz are considered together (respectively in subplots of (a) and (b) in the figures 6, 7, and 8). To allow room for inspection, the vibration amplitude for all three flow rates changes from 0.1 mm to 1 mm at 10 Hz, and from 0.2 mm to 1 mm at 60 Hz. By increasing the amplitude, the lower values of measured heat flux for most data points indicates that the vibration amplitude itself impedes the heat transfer rate. It should be noted that the effect is more visible at lower excess temperatures (i.e. less than 30 ˚C) for flow rates of 140 $\mathrm{ml/min}$ and 160 $\mathrm{ml/min}$ at 10 Hz, which adversely affects the incipient nucleate boiling regime. To support this claim, see the reductions in the heat flux in 6a (i.e.: -14.9% at 9.3 ˚C), and in 7a (i.e. -18.1% at 14.7 ˚C), whereas there is only a subtle decrease in the heat flux of 180 $\mathrm{ml/min}$ in Figure 8a.

By increasing the amplitude from 0.2 mm to 1 mm at the higher frequency of 60 Hz, there is a similar trend for the flow rate of 160 $\mathrm{ml/min}$. At the low excess temperature of 15.9 ˚C for mass flow rate of 180 $\mathrm{ml/min}$, vibration increases heat flux. This reverse trend, with the noticeable heat transfer increase of +13.6% can be attributable to the faster periodic change in the target surface height (with respect to the spray flow field), owing to the 1 mm vibration amplitude, which also influences spray angle. As was explained in the previous section, for the mass flow rate of 180 $\mathrm{ml/min}$ at nozzle height of 21 mm, there was a threshold adversely affecting the heat transfer rate that was attributed to the resultant change in the spray angle. To explain this, as can be seen in Figure 8a, compared to the trend of the boiling curves for the lower flow rates at 10 Hz, the effect of heat transfer attenuation owing to amplitude has been weakened. In this particular case, therefore, this conjecture has credibility, in that at a higher frequency of 60 Hz, the faster change in amplitude (i.e. ±1 mm) and consequently having shorter periods of impeding spray angle, enhance the average local heat flux.

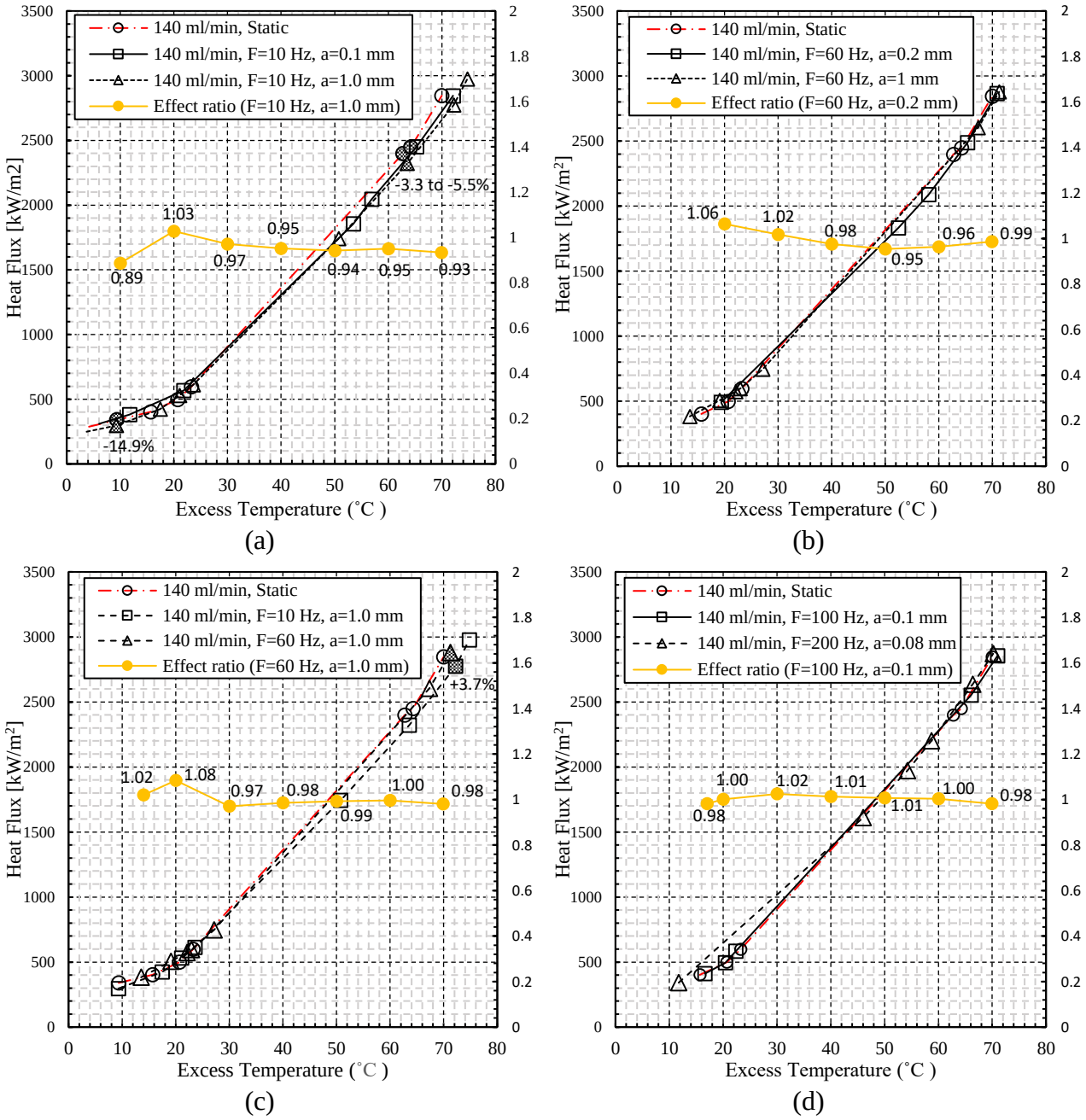

Fig. 6. Nucleate boiling curves with and without vibration for the flow rate of 140 ml/min.

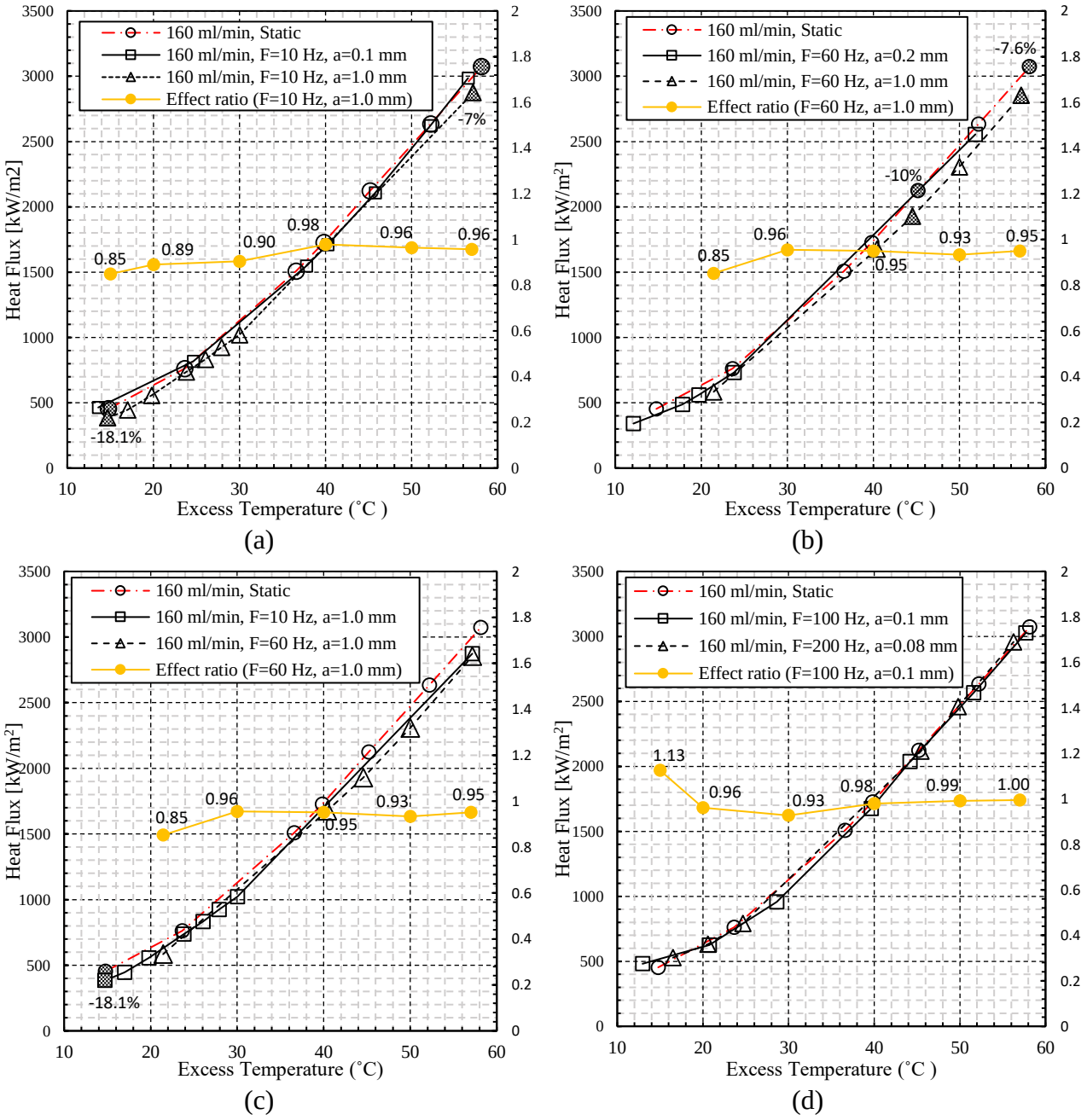

Fig. 7. Nucleate boiling curves with and without vibration for the flow rate of 160 ml/min.

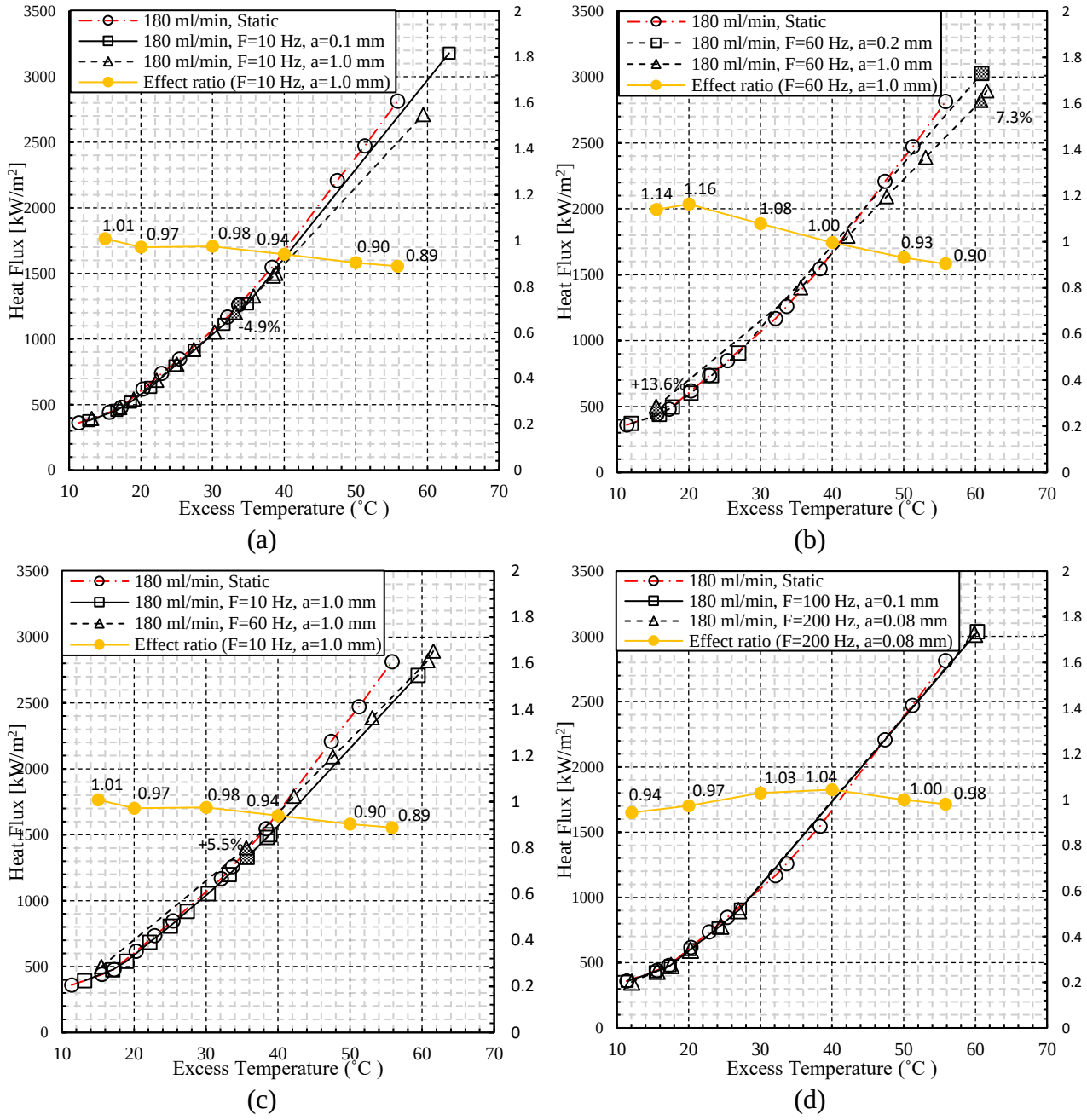

Fig. 8. Nucleate boiling curves with and without vibration for the flow rate of 180 ml/min.

By contrast, subplots Figure 6c, Figure 6d, Figure 7c, Figure 7d, Figure 8c, and Figure 8d demonstrate the influence of frequency on the heat flux at fixed amplitudes of 0.08, 0.1, and 1 mm for step changes in frequency of 10 to 60 Hz and 100 to 200 Hz. Considering the step change of 10 Hz to 60 Hz, there are only two visible enhancement effects in flow rates of 140 $\mathrm{ml/min}$ and 180 $\mathrm{ml/min}$. As can be seen in Figure 7c, at 140 $\mathrm{ml/min}$ the higher frequency of 60 Hz around an excess temperature of 72 ˚C, contributes to heat transfer enhancement (of 3.7%), compared to that for a lower frequency of 10 Hz. A heat transfer enhancement of 5.5% is observed at the flow rate of 180 $\mathrm{ml/min}$ around an excess temperature of 35.5 ˚C. The reason for this increase in heat flux for a higher frequency (from 10 to 60 Hz) at a fixed amplitude, is due in part to the enhanced vibrational Reynolds number ($Re_V = \rho_l a \omega d_H / \mu_l$) promoting the turbulence. Additionally, the resulting

acceleration in the liquid film plays a prominent role in providing better liquid drainage [46] and a thinner layer on top of the surface, thereby reducing thermal insulation. This claim can be supported by the fact that the dimensionless acceleration ($\omega^2 a/g$) increases in proportion to the frequency squared.

Further inspection of the plots shows no visible change in the heat flux by the step change in higher range frequencies of 100 Hz to 200 Hz. This observation is not inconsistent with the previous conclusion because the effect of vibration in the presented range of amplitude and frequency is in general impeding. At this step change for all flow rates, the trend shows a convergence to the results of *static* cases. Therefore, in comparison with the results under low frequency vibration versus the *static* case, no change in the heat flux for the higher frequencies (over *static*) offers an improvement by the increased Reynolds number and acceleration.

5.2.2 The effect of high-frequency low-amplitude surface vibration on heat flux

To understand how frequency can affect the trend of the nucleate boiling curve, results with low amplitude of 0.02 mm, and three high frequencies of 100, 200, and 400 Hz are shown in Figure 9, Figure 10, and Figure 11. The results for the nozzle-to-surface distances of 17 mm and 21 mm are given. For the nozzle height of 21 mm, considering the lower flow rates of 140 $\mathrm{ml/min}$, the results are given in Figure 9b, and for 160 $\mathrm{ml/min}$ in Figure 10b. Across all the excess temperature regions, the heat-flux does not follow the changes in frequency, although a small decrease in heat-flux from increasing frequency is evident in the results for the lower excess temperature regions (i.e. below 30 ˚C). By contrast, for excess temperature above 30 ˚C, the gradient of the heat flux as a function of excess temperature is similar for all frequencies. This effect becomes more intense with a higher flow-rate of $180\ \mathrm{ml/min}$ as shown in Figure 11b, as the gaps between the curves increase with an increase in frequency and excess temperature (up to 8.2% in Figure 11b). This clearly indicates that there is a definite effect of frequency on the heat transfer, which can be either enhancement or attenuation depending on the mechanism of nucleation.

Exploring the effect of high frequency vibrations on the trend for the lower nozzle height of 17 mm, Figure 9a, Figure 10a, Figure 11a and Figure 11c show that high frequency makes the attenuation effect more evident. For lower excess temperatures in which nucleation is the primary mechanism, by increasing the frequency the most heat transfer attenuation of -30.1% occurs for the lowest mass flow rate of 140 $\mathrm{ml/min}$ at the lowest excess temperature of 10 ˚C. This is because of suppressed bubbles which are generated on the surface within the liquid film by the high acceleration of 12.9 g from the high frequency vibration. Inducing such a force can delay the departure of the bubbles from the surface, and in turn, the trapped bubbles reduce the density of nucleate sites, which subsequently cause a significant heat flux reduction. Nevertheless, from the higher flow rates of 160 $\mathrm{ml/min}$ to 200 $\mathrm{ml/min}$ as shown in Figure 11c, this hindrance to the departure of bubbles is weakened by a more powerful penetration effect of the droplets which were strengthened by a higher flow rate. Therefore, the impeding effect of high frequency vibration has disappeared from the trend. For the higher excess temperature regions, from the lowest flow rate to the maximum of 200 $\mathrm{ml/min}$, the difference between the heat flux values (corresponding to cases with and without vibration) increases, giving rise to heat transfer rate reduction of -3.6% in Figure 10a. This is because of the impeding effect of high acceleration on the departure of the bubbles, which occurs when the penetration force of the high velocity droplets is no longer able to improve the density of the nucleate sites. The bubbles at the higher surface temperatures start to accumulate and develop small slugs which adversely affect the heat transfer rate [5].

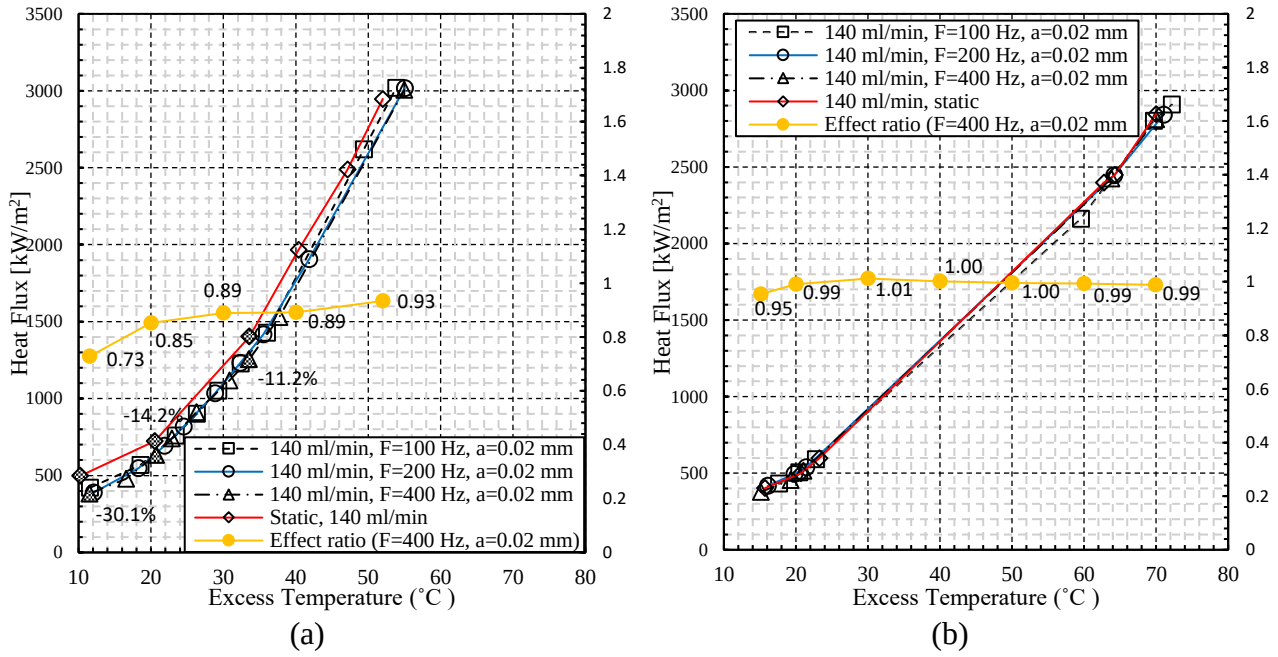

Fig. 9. Heat flux over the excess temperature for *static* and *Dynamic* test runs with the amplitude of 0.02 mm and frequencies up to 400 Hz for nozzle heights of: a) H =17 mm b) H =21 mm

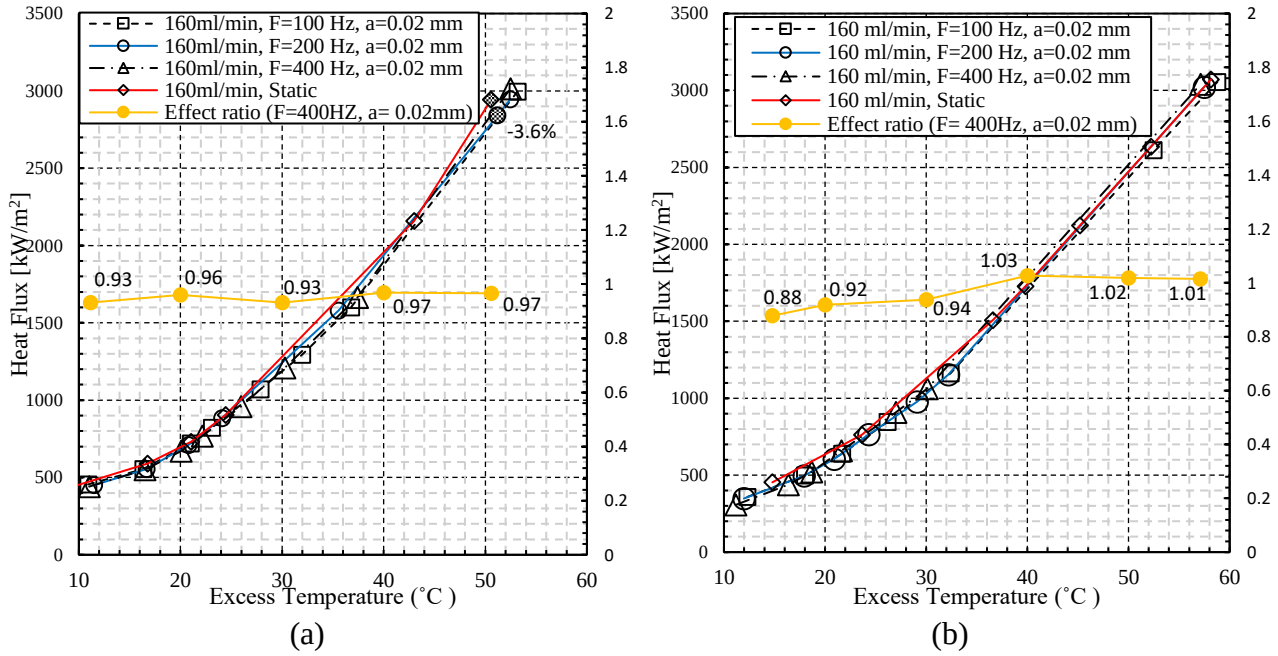

Fig. 10. Heat flux over excess temperature for *static* and *Dynamic* test runs with the amplitude 0.02 mm and frequencies up to 400 Hz: (a) v =160ml/min and H =17mm (b) v =160ml/min and H =21mm

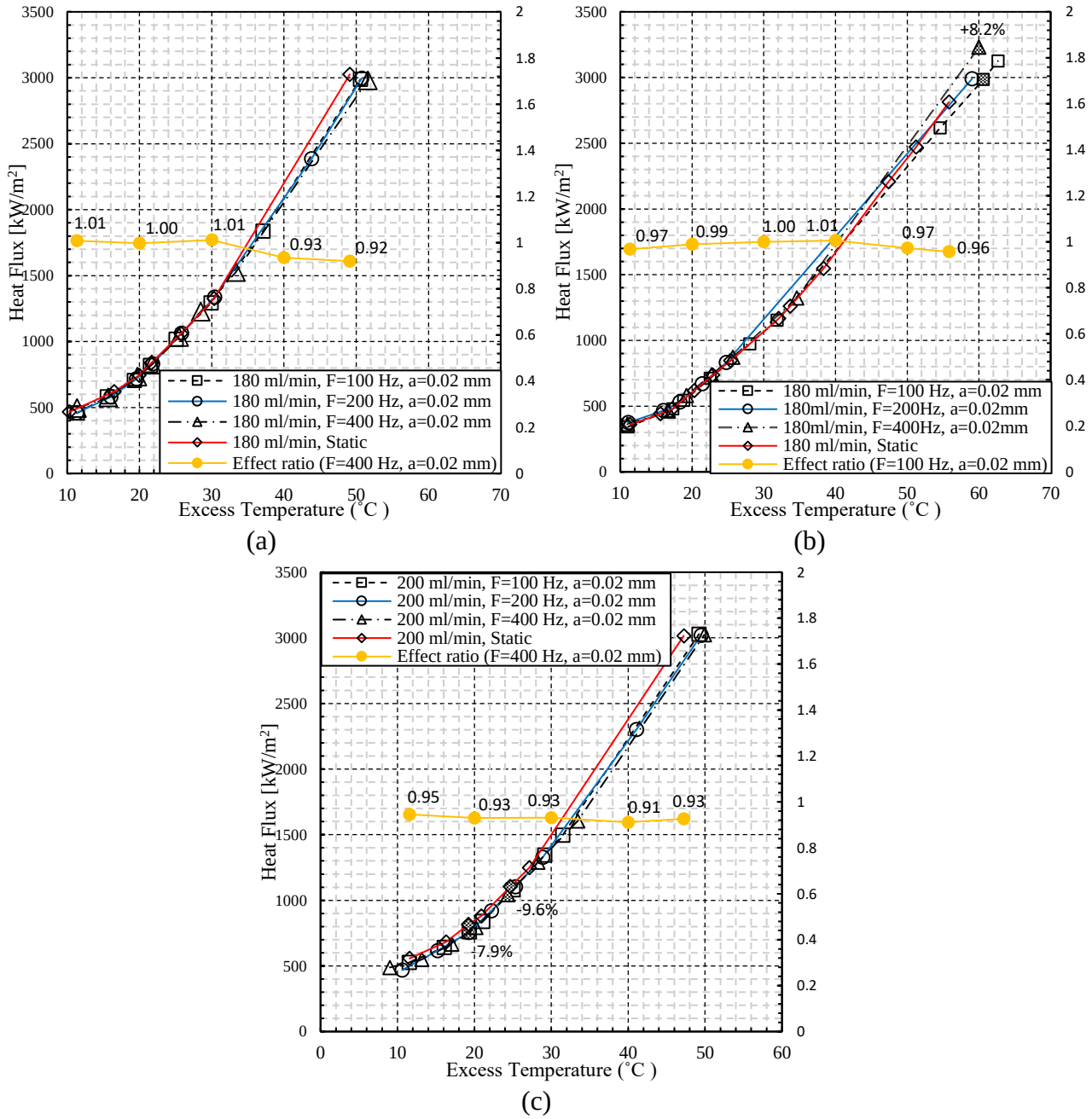

Fig. 11. Heat flux over excess temperature for *static* and *Dynamic* tests with an amplitude of 0.02 mm and frequencies up to 400 Hz: (a) v =180ml/min and H =17mm, (b) v =180ml/min and H =21mm, (c) v =200ml/min and H =17mm

5.2.3 The effect of low-frequency high-amplitude surface vibration on heat flux

The results so far have shown the effect of low amplitude vibration on spray cooling for middle range and high frequency test runs. The trend for each flow rate was found to be highly dependent on the complex relationship between frequency, amplitude, and excess temperature, since it is always either enhancing or attenuating the effect in the lower and higher surface temperature regions. It would therefore be expected that there should be an optimum value of heat flux. Higher amplitudes are needed to assess the sensitivity of such an important parameter, which is important for design in application areas with dynamic conditions (e.g. thermal management of Range

Extenders and power electronics in hybrid electric vehicles [9]). In this regard, 21 tests involving vibrations with the largest amplitude possible (i.e. up to 12 mm) corresponding to typical road test conditions have been run. The results are shown in Figure 12. By increasing the vibration amplitude, the trend shows interesting behaviour for different volumetric flow rates. At large values of excess temperature i.e. $\Delta T > 40$ ˚C, the difference between heat flux values at the same excess temperatures associated with *dynamic* vibration amplitudes up to 8 mm, and the *static* case, gradually decreases by varying the flow rate from 160 $\mathrm{ml/min}$ to 200 $\mathrm{ml/min}$. By contrast, a reverse trend is evident, for the largest amplitude as the flow rate increases, when the heat flux is compared to the *static* case, as now explained in more detail.

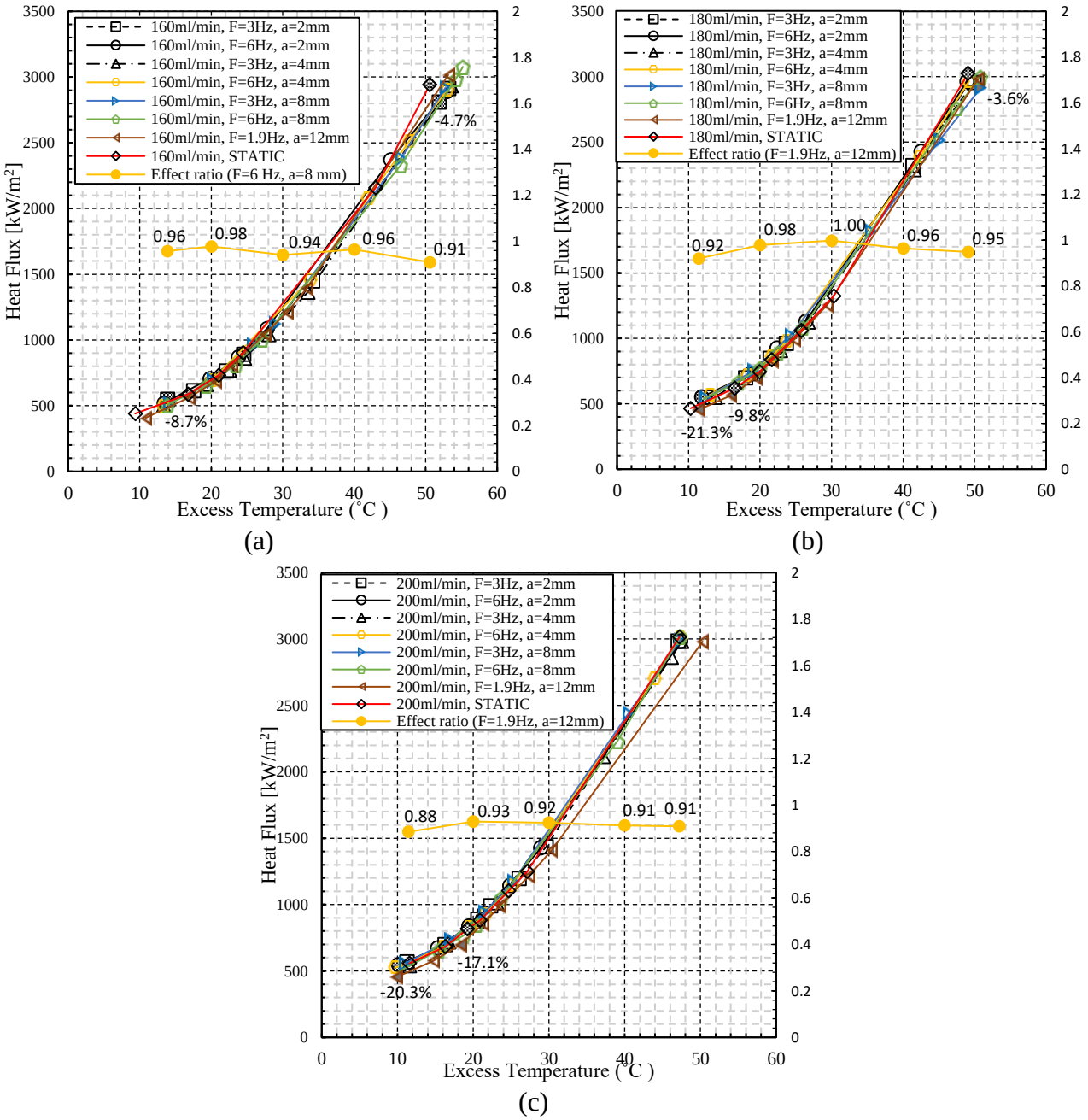

Fig. 12. Performance boiling curves for large amplitude vibrations at the nozzle height of 17mm

To explain the trend observed, the dimensionless acceleration and the vibrational Reynolds number for all the large amplitude vibration cases are supplied in Table 7 (each row represents the same case in the legends of the figures). By increasing the flow rate, the cases with lower acceleration, and a Vibrational Reynolds Number up to 10250, follow the same behaviour; i.e. the difference between these dynamic cases and the *static* case finally converge at a particular flow rate. There is obviously a trade-off between the attenuating effect of vibration and the enhancing influences of acceleration and flow rate. Considering cases Number 4 and 5 in Table 7 with a similar Vibrational Reynolds Number around 10250 but a lower acceleration for case Number 5, the performance curve of Case Number 5 converges at a higher flow rate of 200 $\mathrm{ml/min}$. By contrast, the boiling curve for Case Number 4 converges to the *static* performance curve at 180 $\mathrm{ml/min}$. Furthermore, the curve for the largest amplitude case of 12 mm, with a smaller acceleration of 0.17 g, and a Vibrational Reynolds Number around 9740 (which is not very different from 10250), compared to Cases 4 and 5, has not yet converged at the flow rate of 200 $\mathrm{ml/min}$. Therefore, the reverse trend mentioned for the largest amplitude is now consistent with the conclusion. Deductions from performance curves are used in the next section to evaluate how the fitted correlation data emulate the effect of varying the key parameters.

Table 7. Acceleration and Vibrational Reynolds number for the large amplitude vibration test runs.

Test case	Frequency (Hz)	Amplitude (mm)	Acceleration (unit of g)	Vibrational Reynolds Number
1	3	2	0.072	2560
2	6	2	0.289	5130
3	3	4	0.145	5130
4	6	4	0.579	10250
5	3	8	0.289	10250
6	6	8	1.159	20500
7	1.9	12	0.174	9740

6 Correlation models

In choosing a reliable and applicable correlation model either for the purpose of design or for thermal management of a hybrid electric vehicle cooling system, three issues are important. First it is important for the correlation to be valid in the range of the desired operational conditions. Second the reliability of the correlation model should be checked to establish the error band with which the correlation model is able to predict the experimental data (by comparison to the model accuracies shown in Table 1). Third, precision measuring instruments themselves add some uncertainty to the measured empirical data. The uncertainty of measured experimental data can be undertaken using the method proposed by Moffat [48]. All the available correlations in nucleate boiling regime are classified in Table 1, allowing different models to be chosen based on their operational conditions and experimental uncertainties, as well as modelling or data fitting errors. (Only the reported limitations are given in Table 1 since the operational conditions are reported with different hydrodynamic parameters).

For the specific aim of thermal management, owing to the undetectable variability in machining, the flow field of spray might differ, resulting in a sizeable error associated with using correlations. This may be the case even if the particular nozzle used, is consistent with information reported in the literature. Considering this, there are concerns about using spray flow data from one nozzle to

predict the heat transfer characteristics of a different nozzle, even if they have the same geometry. Overall, the ideal solution is to use the same nozzle [38] to obtain both the hydrodynamic and heat transfer characteristics, and then try to use a fitting function or any other modelling approach to make a unique correlation for every nozzle.

Here the correlations developed by dimensional analysis and similitude (Table 4) are fitted to the data points. The whole database associated with the case studies of *Static* and *Dynamic* is considered for the data fitting. The best root-mean-square error and average deviation for both *Static* and *Dynamic* cases was calculated using a nonlinear data fitting method via least square regression with an optimisation option of 'bisquare' for robustness, using the Levenberg-Marquardt algorithm. Only the results using this option are presented. For the current study, which has invariant parameters of chamber pressure and subcooling degree, the fitting functions (for both cases) from Table 3 has been chosen.

For *static* results, Figure 13a shows the experimental results over the predicted data points using the chosen fitting function according to:

$$Bo = 3.87 \times 10^{-2} Ja^{1.5573} \left(\frac{\rho_l^2 \sigma v}{{\mu_l}^3}\right)^{0.5008} \quad (8)$$

where Bo is Boiling number ($qH/\mu_l h_{fg}$) and Ja is Jacob number ($Ja = C_l \Delta T/h_{fg}$), which gives the ratio of the sensible heat to the latent heat.

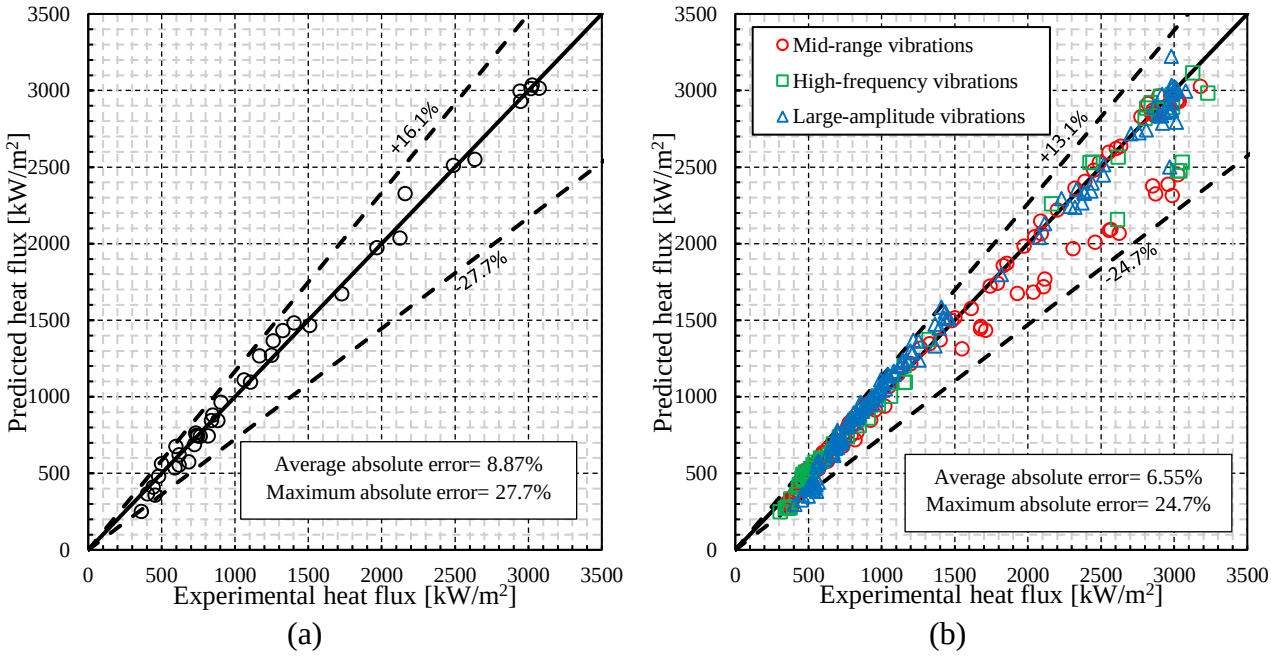

Fig. 13. Results predicted by correlations with the error windows: (a) *static* and (b) d*ynamic*.

For measured *Dynamic* data, three ranges of high frequency and amplitude respectively within the range 1.9 Hz to 400 Hz, and 0.02 mm to 12 mm, cover an operating region (as shown in Table 5). Figure 13b shows for the dynamic measurements, the predicted results over the experimentally-measured data based on a fitted correlation model:

$$Bo = 1.24 \times 10^{-2} Ja^{1.3920} \left(\frac{\rho_l^2 \sigma v}{{\mu_l}^3}\right)^{0.9809} Re_V^{-0.9869} \left(\frac{a}{H}\right)^{0.4825} Ac^{0.4998} \quad (9)$$

where $Re_V = \rho_l a \omega d_H / \mu_l$, the Vibrational Reynolds Number is used for the first time, which includes both the amplitude and frequency effects on the heat transfer rate. $Ac = \omega^2 a/g$, is the Dimensionless Acceleration Number.

6.1 Discussion of the fitted correlation models

For the *static* correlation model comparison, all the predicted results (of 42 data points) are shown between the error windows of -27.7% and +16.1%, with an average absolute error of 8.87%. The maximum absolute error occurred in the predicted data obtained for the data point with the lowest heat flux of 360 $\mathrm{kW/m^2}$at the flow rate of 180 ml/min (nozzle height of 17mm in Fig. 3). As was mentioned previously, this flow rate had a reverse trend, which could be a reason for adversely affecting the prediction. Nonetheless, considering the low number of data points, and consequently low resolution in the *static* database, the correlation prediction quality comparing to the rest of the available models is of acceptable quality (with reference to the error bands in Table 1).

For the *dynamic* correlation model comparison, which is based on Vibrational Reynolds Number and acceleration, demonstrates reasonable prediction capability with average and maximum absolute errors of 6.55% and 24.7% respectively. The underestimation of -24.7% is mostly related to the mid-range vibrations for heat fluxes above 1500 $\mathrm{kW/m^2}$. For the large amplitude low frequency vibration results (which are important for the thermal management in hybrid electric vehicles), most of the scatter (i.e. underestimation and overestimation of +13.1%) is related to heat flux less than 1500 $\mathrm{kW/m^2}$. However, for most cooling systems, higher heat removal is important to keep the surface temperature within a safe temperature range. Furthermore, since the correlation is concise and flexible enough to easily update its empirical coefficients (such as being needed to fit the model for use with other nozzles and operating conditions), the models fitted here offer potentially promising application to future model-based spray evaporative cooling control systems [14, 55].

Further improvement can be obtained by allocating a dynamic model to each mechanical vibration range, i.e. Mid-amplitude range (a = 0.08 - 1 mm, f=10 - 200 Hz), High-frequency (a=0.02 mm, f=100 - 400 Hz); and Large-amplitude range (a = 2 -12 mm, f=1.9 - 6 Hz). After nonlinear model fitting to the measured data, new parameters associated with each range plus corresponding prediction errors are listed in Table 8. As can be seen, the average absolute deviations and the maximum absolute errors are all improved in comparison to the values obtained for the whole range. Figure 14 shows the predicted results for the experimentally-measured data in each range. The prediction errors for each window are all reduced in comparison with the errors for the entire range.

Table 8. Dynamic correlation parameters and prediction errors for different vibration ranges - Dynamic correlation model $Bo = a\,Ja^{b}(\frac{\rho_l^2\sigma v}{\mu_l{}^3})^{c}Re_V^{d}\left(\frac{a}{H}\right)^{e}Ac^{f}$, Parameters: a, b, c, d, e, f.

Vibration range	Parameters						Average of the absolute error (%)	Maximum absolute error (%)
	a	b	c	d	e	f		
Whole	0.0124	1.3920	0.9809	-0.9869	0.4825	0.4927	6.55	24.7
Mid	0.016	1.3803	0.9837	-1.0347	0.5036	0.5245	2.40	22.4
High-frequency	0.00048	1.3822	1.0580	-0.4894	0.7811	0.2453	1.00	22.2
Large-amplitude	0.0005	1.4540	0.8826	-0.4544	0.2040	0.2376	3.06	23.2

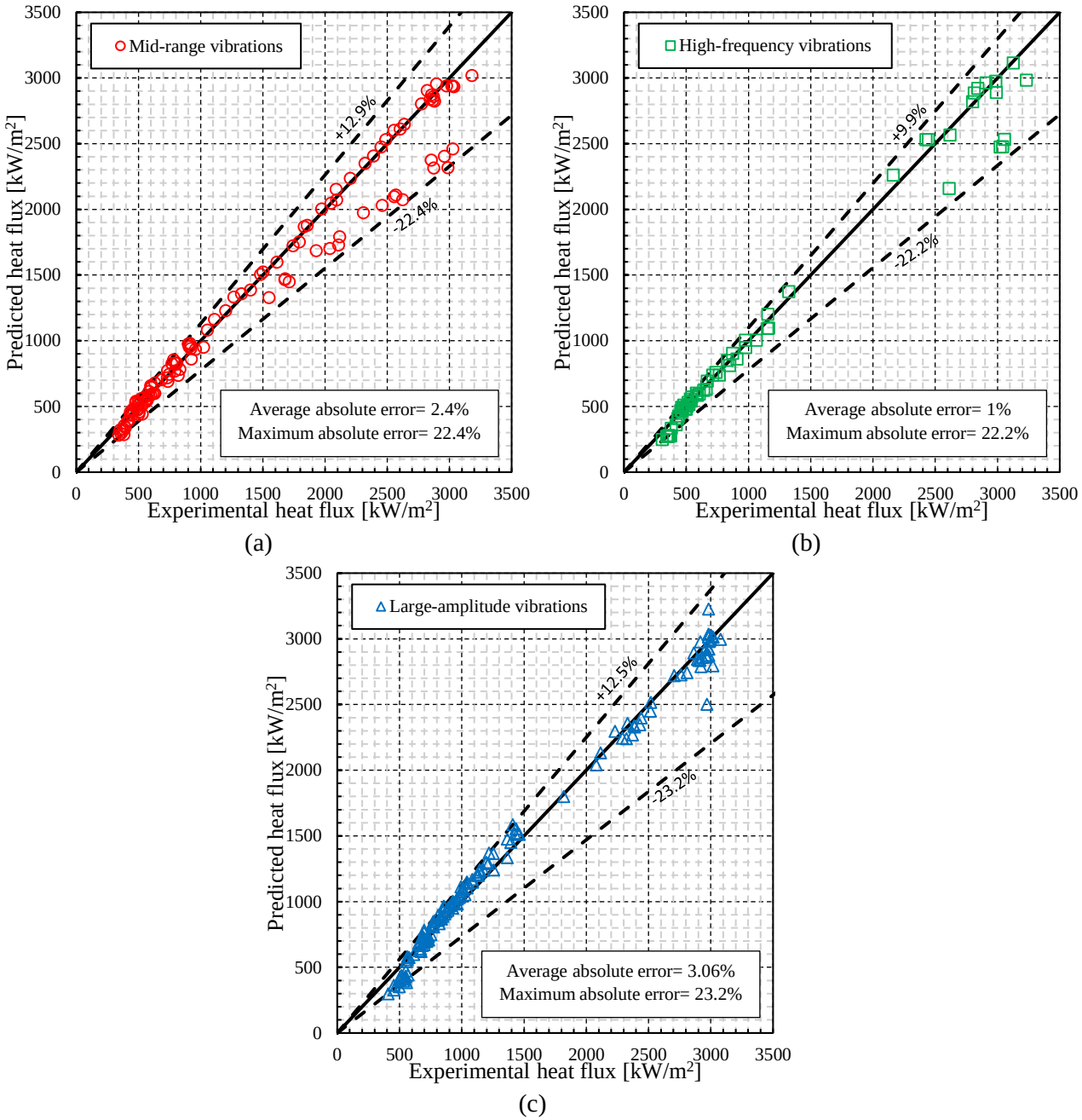

Fig. 14. Improved dynamic correlations for vibration ranges: (a) *Mid-range*, (b) *High-frequency* and (c) Large-amplitude.

7 Conclusions

The effect of dynamic behaviour on the nucleate boiling regime of spray evaporative cooling of a horizontal flat test piece with, and without vibration, has been examined using measured data, and appropriate dynamic correlation models have been developed and adopted. The flat test piece was excited by a shaker with water coolant supplied to the vibrating heated surface via a spray nozzle. Comprehensive dimensional and similitude analysis was first undertaken to develop dynamic correlation models, and to design a suitable experimental measurement programme. Using a full-cone nozzle, four volumetric flow rates of 140 $\mathrm{ml/min}$, 160 $\mathrm{ml/min}$, 180 $\mathrm{ml/min}$ and 200 $\mathrm{ml/min}$ were tested. These flow rates are shown to be dependent on the range of vibrations, and the heights of the nozzles. Three sets of dynamic conditions have been investigated including a 'mid-range' frequency, a 'high' frequency, and large-amplitude vibrations at 'low' frequency. For the mid-range vibrations at frequencies from 10 Hz to 200 Hz, the amplitudes vary from 0.08 mm to 1 mm. Three high-frequency vibration test were undertaken at 100 Hz, 200 Hz, and 400 Hz, with a fixed amplitude of 0.02 mm, and varying flow rates of 140, 160, 180, and 200 $\mathrm{ml/min}$, at nozzle distances above the test piece of 17mm and 21mm. Large-amplitude vibration tests were undertaken at frequencies of 1.9 Hz, 3 Hz, and 6 Hz, with amplitudes varying from 2 mm to 12 mm (emulating conditions associated with real vehicle dynamics) where the nozzle-to-surface distance was 17 mm, giving the highest effective flow rate. The main conclusions are:

- Any increase in volumetric flow-rate, under both *Static* and *Dynamic* conditions, was found to cause heat transfer coefficient enhancement, except for a flow rate of 180 $\mathrm{ml/min}$, at a nozzle height of 21 mm, where a reverse trend occurred. The reason for this reverse trend can be attributed to an increase in spray cone-angle with increasing flow-rate. Below a nozzle-specific cone angle threshold, heat flux increases with cone-angle. But when this threshold is exceeded, heat flux declines with further increase in cone-angle.
- For the mid-range vibration frequencies from 10 Hz to 200 Hz, the amplitude in general impedes the heat transfer rate, while the effect is more visible on the lower excess temperatures (less than 30 ˚C). Increasing frequency augments the heat transfer by the increased Reynolds number and acceleration. However, the effect of vibration generally results in an attenuation in heat transfer compared with *static* cases. Several mechanisms have been identified as the reason depending on the vibration amplitude and frequency, flow rate, and excess temperature. At low amplitude, high frequency vibration, high surface acceleration causes bubble suppression which influences nucleate boiling, particularly for low flow rate. At high amplitude, low frequency vibration, there are two opposing effects associated with increasing dimensionless acceleration which enhances heat transfer, and increasing Vibrational Reynolds Number, which suppresses heat transfer and proves to be more dominant.
- For high-frequency vibration, the heat transfer decline occurs more prominently for the lower nozzle height of 17 mm compared to the higher nozzle height of 21 mm. The maximum heat flux of -30.1% occurred for the lowest flow rate of 140 $\mathrm{ml/min}$ at the lowest level of 'superheating' of 10 ˚C. The reason appears to be that lower nozzle heights have greater sensitivity to bubble suppression, which influences nucleate boiling causing a reduction in heat transfer.

- A performance evaluation of large-amplitude vibrations demonstrated that there is a balance between the attenuating effect of vibration and the enhancing influences of acceleration and flow rate.
- The results of the deriving and fitting new dynamic correlation models shows very reasonable prediction quality, which can be reliably used for future model-based thermal management applications.

Conflict of Interest

The authors have no conflict of interest to declare in the submission of this research paper.

Acknowledgements

The authors wish to acknowledge the financial and technical support of Ricardo Shoreham Technical Centre, UK.

References

[1] J. Kim, J. Oh, H. Lee, Review on battery thermal management system for electric vehicles, Applied Thermal Engineering, 149 (2019) 192-212.
[2] J. Benajes, A. García, J. Monsalve-Serrano, S. Martínez-Boggio, Emissions reduction from passenger cars with RCCI plug-in hybrid electric vehicle technology, Applied Thermal Engineering, 164 (2020) 114430.
[3] Z. Mera, N. Fonseca, J.-M. López, J. Casanova, Analysis of the high instantaneous NOx emissions from Euro 6 diesel passenger cars under real driving conditions, Applied energy, 242 (2019) 1074-1089.
[4] S. Tsiakmakis, G. Fontaras, J. Dornoff, V. Valverde, D. Komnos, B. Ciuffo, P. Mock, Z. Samaras, From lab-to-road & vice-versa: Using a simulation-based approach for predicting real-world CO2 emissions, Energy, 169 (2019) 1153-1165.
[5] J. Breitenbach, I.V. Roisman, C. Tropea, From drop impact physics to spray cooling models: a critical review, Experiments in Fluids, 59(3) (2018) 55.
[6] G. Liang, I. Mudawar, Review of spray cooling–Part 1: Single-phase and nucleate boiling regimes, and critical heat flux, International Journal of Heat and Mass Transfer, 115 (2017) 1174-1205.
[7] G. Liang, I. Mudawar, Review of spray cooling–Part 2: High temperature boiling regimes and quenching applications, International Journal of Heat and Mass Transfer, 115 (2017) 1206-1222.
[8] S. Jafari, J.F. Dunne, M. Langari, Z. Yang, J.-P. Pirault, C.A. Long, J. Thalackottore Jose, A review of evaporative cooling system concepts for engine thermal management in motor vehicles, Proceedings of the Institution of Mechanical Engineers, Part D: Journal of Automobile Engineering, 231(8) (2017) 1126-1143.
[9] I. Mudawar, D. Bharathan, K. Kelly, S. Narumanchi, Two-phase spray cooling of hybrid vehicle electronics, IEEE Transactions on Components and Packaging Technologies, 32(2) (2009) 501-512.
[10] J.T. Jose, J.F. Dunne, J.-P. Pirault, C.A. Long, Spray Evaporative Cooling System Design for Automotive Internal Combustion Engines, in: ASME 2018 Internal Combustion Engine Division Fall Technical Conference, American Society of Mechanical Engineers, 2018, pp. V002T007A008-V002T007A008.
[11] X. Feng, S. Zheng, D. Ren, X. He, L. Wang, X. Liu, M. Li, M. Ouyang, Key characteristics for thermal runaway of li-ion batteries, Energy Procedia, 158 (2019) 4684-4689.

[12] Y. Xie, X.-j. He, X.-s. Hu, W. Li, Y.-j. Zhang, B. Liu, Y.-t. Sun, An improved resistance-based thermal model for a pouch lithium-ion battery considering heat generation of posts, Applied Thermal Engineering, 164 (2020) 114455.
[13] J. Du, Y. Liu, X. Mo, Y. Li, J. Li, X. Wu, M. Ouyang, Impact of high-power charging on the durability and safety of lithium batteries used in long-range battery electric vehicles, Applied Energy, 255 (2019) 113793.
[14] S. Jafari, J.F. Dunne, M. Langari, Z. Yang, J.-P. Pirault, C.A. Long, J.T.J.J.o.T.S. Jose, E. Applications, Control of Spray Evaporative Cooling in Automotive Internal Combustion Engines, 10(4) (2018) 041011.
[15] M.R. Panão, A.L. Moreira, Intermittent spray cooling: a new technology for controlling surface temperature, International Journal of Heat and Fluid Flow, 30(1) (2009) 117-130.
[16] H. Bostanci, S. Altalidi, S. Nasrazadani, Two-phase spray cooling with HFC-134a and HFO-1234yf on practical enhanced surfaces, Applied Thermal Engineering, 131 (2018) 150-158.
[17] W.-L. Cheng, W.-W. Zhang, H. Chen, L. Hu, Spray cooling and flash evaporation cooling: the current development and application, Renewable and Sustainable Energy Reviews, 55 (2016) 614-628.
[18] Z.-F. Zhou, Y.-K. Lin, H.-L. Tang, Y. Fang, B. Chen, Y.-C. Wang, Heat transfer enhancement due to surface modification in the close-loop R410A flash evaporation spray cooling, International Journal of Heat Mass Transfer, 139 (2019) 1047-1055.
[19] Y.-K. Lin, Z.-F. Zhou, Y. Fang, H.-L. Tang, B. Chen, Heat transfer performance and optimization of a close-loop R410A flash evaporation spray cooling, Applied Thermal Engineering, 159 (2019) 113966.
[20] H. Liu, C. Cai, M. Jia, J. Gao, H. Yin, H. Chen, Experimental investigation on spray cooling with low-alcohol additives, Applied Thermal Engineering, 146 (2019) 921-930.
[21] J. Yang, L. Chow, M. Pais, Nucleate boiling heat transfer in spray cooling, Journal of Heat Transfer, 118(3) (1996) 668-671.
[22] D.P. Rini, R.-H. Chen, L.C. Chow, Bubble behavior and nucleate boiling heat transfer in saturated FC-72 spray cooling, Journal of Heat Transfer, 124(1) (2002) 63-72.
[23] S.K. Mishra, A. Arora, H. Chandra, Application of Vibration on Heat Transfer-A Review, i-Manager's Journal on Future Engineering and Technology, 15(1) (2019) 72.
[24] A. Sathyabhama, S. Prashanth, Enhancement of boiling heat transfer using surface vibration, Heat Transfer—Asian Research, 46(1) (2017) 49-60.
[25] Z. Wang, Y. Xing, X. Liu, L. Zhao, Y. Ji, Computer modeling of droplets impact on heat transfer during spray cooling under vibration environment, Applied Thermal Engineering, 107 (2016) 453-462.
[26] C. Tropea, I.V. Roisman, Modeling of spray impact on solid surfaces, Atomization and sprays, 10(3-5) (2000).
[27] S.-S. Hsieh, G.-W. Chen, Y.-F. Yeh, Optical flow and thermal measurements for spray cooling, International Journal of Heat and Mass Transfer, 87 (2015) 248-253.
[28] E. Cabrera, Heat flux correlation for spray cooling in the nucleate boiling regime, Experimental heat transfer, 16(1) (2003) 19-44.
[29] Y. Tan, J. Xie, F. Duan, T. Wong, K. Toh, K. Choo, P. Chan, Y. Chua, Multi-nozzle spray cooling for high heat flux applications in a closed loop system, Applied thermal engineering, 54(2) (2013) 372-379.
[30] L. Ortiz, J.E. Gonzalez, Experiments on steady-state high heat fluxes using spray cooling, Experimental Heat Transfer, 12(3) (1999) 215-233.
[31] M.S. Sehmbey, L.C. Chow, O.J. Hahn, M.R. Pais, Effect of spray characteristics on spray cooling with liquid nitrogen, Journal of Thermophysics and heat Transfer, 9(4) (1995) 757-765.
[32] S.-S. Hsieh, T.-C. Fan, H.-H. Tsai, Spray cooling characteristics of water and R-134a. Part II: transient cooling, International Journal of Heat and Mass Transfer, 47(26) (2004) 5713-5724.
[33] M. Ghodbane, J.J.I.J.o.H. Holman, M. Transfer, Experimental study of spray cooling with Freon-113, 34(4-5) (1991) 1163-1174.
[34] J.R. Rybicki, I. Mudawar, Single-phase and two-phase cooling characteristics of upward-facing and downward-facing sprays, International Journal of Heat and Mass Transfer, 49(1-2) (2006) 5-16.
[35] R.H. Pereira, E.P.B. Filho, S.L. Braga, J.A.R. Parise, Nucleate boiling in large arrays of impinging water sprays, Heat Transfer Engineering, 34(5-6) (2013) 479-491.
[36] R. Dou, Z. Wen, G. Zhou, Heat transfer characteristics of water spray impinging on high temperature stainless steel plate with finite thickness, International Journal of Heat and Mass Transfer, 90 (2015) 376-387.

[37] Y. Qiao, S. Chandra, Spray cooling enhancement by addition of a surfactant, Journal of Heat Transfer, 120(1) (1998) 92-98.
[38] I. Mudawar, W. Valentine, Determination of the local quench curve for spray-cooled metallic surfaces, Journal of Heat Treating, 7(2) (1989) 107-121.
[39] G. Bluman, Dimensional analysis, modelling and symmetry, International Journal of Mathematical Education in Science and Technology, 14(3) (1983) 259-272.
[40] E. Buckingham, Model experiments and the forms of empirical equations, Verlag nicht ermittelbar, 1915.
[41] E. Buckingham, On physically similar systems; illustrations of the use of dimensional equations, Physical review, 4(4) (1914) 345.
[42] A. Flaga, Basic principles and theorems of dimensional analysis and the theory of model similarity of physical phenomena, Czasopismo Techniczne, (2015).
[43] A.A. Sonin, A generalization of the Π-theorem and dimensional analysis, Proceedings of the National Academy of Sciences, 101(23) (2004) 8525-8526.
[44] Z. Wang, Y. Xing, X. Liu, L. Zhao, Yibin Ji, Computer modeling of droplets impact on heat transfer during spray cooling under vibration environment, Applied Thermal Engineering. 107 (2016) 453-462.
[45] H. Atashi, A. Alaei, M. Kafshgari, R. Aeinehvand, S. Rahimi, New Pool Boiling Heat Transfer in the Presence of Low-Frequency Vibrations Into a Vertical Cylindrical Heat Source, Experimental Heat Transfer, 27(5) (2014) 428-437.
[46] Y. Zhang, L. Pang, M. Liu, Y. Xie, Investigation of spray cooling: Effect of different heater surfaces under acceleration, International Communications in Heat and Mass Transfer, 75 (2016) 223-231.
[47] K.-i. Yoshida, Y. Abe, T. Oka, Y.H. Mori, A. Nagashima, Spray cooling under reduced gravity condition, Journal of heat transfer, 123(2) (2001) 309-318.
[48] K. Baysinger, K. Yerkes, R. Harris, T. Michalak, J. McQuillen, Design of a microgravity spray cooling experiment, in: 42nd AIAA Aerospace Sciences Meeting and Exhibit, 2004, pp. 966.
[49] K. Sone, K. Yoshida, T. Oka, Y. Abe, Y. Miri, A. Nagashima, Spray cooling characteristics of water and FC-72 under reduced and elevated gravity for space application, in: IECEC 96. Proceedings of the 31st Intersociety Energy Conversion Engineering Conference, IEEE, 1996, pp. 1500-1505.
[50] R.J. Moffat, Describing the uncertainties in experimental results, Experimental thermal and fluid science, 1(1) (1988) 3-17.
[51] J. Schwarzkopf, T. Cader, K. Okamoto, B. Li, B. Ramaprian, Effect of spray angle in spray cooling thermal management of electronics, in: ASME 2004 Heat Transfer/Fluids Engineering Summer Conference, American Society of Mechanical Engineers Digital Collection, 2004, pp. 423-431.
[52] I. Mudawar, K. A. Estes, Optimizing and predicting CHF in spray cooling of a square surface, 118(3) (1996) 672-679.
[53] R.-H. Chen, L.C. Chow, J.E. Navedo, Optimal spray characteristics in water spray cooling, International Journal of Heat and Mass Transfer, 47(23) (2004) 5095-5099.
[54] Y. Qiao, S.J.J.o.H.T. Chandra, Spray cooling enhancement by addition of a surfactant, 120(1) (1998) 92-98.
[55] B. Petrus, K. Zheng, X. Zhou, B.G. Thomas, J.J.M. Bentsman, m.t. B, Real-time, model-based spray-cooling control system for steel continuous casting, Metallurgical and materials transactions 42(1) (2011) 87-103.
[56] J. T. Jose, Spray Evaporative Cooling of Vibrating Surfaces with Application to Automotive Combustion Engines, PhD Thesis, University of Sussex, 2020.

Nomenclature

$\dot{m}$	mass flow rate (kg/s)
$\vec{v}$	volumetric spray flux (m^3s^{-1}/m^2)
$\bar{\vec{v}}$	average volumetric spray flux (m^3s^{-1}/m^2)

A	surface area (m^2)
Ac	dimensionless acceleration (units of g)
a	Amplitude of vibration (m)
Bo	Boiling number (-)
C_p	Specific heat (kJ/kg k)
d	Diameter (mm)
d_{05}	mass or volume median diameter (m)
d_{32}	Sauter mean diameter (m)
f	Frequency (Hz)
G	mass velocity ($\mathrm{kg/m^2 s}$)
h	specific enthalpy (kJ/kg)
h	heat transfer coefficient ($\mathrm{kW/m^2\ K}$)
H	height (m)
Ja	Jacob number
k	thermal conductivity (W/m K)
L	length (mm)
P	pressure (kPa)
Pr	Prandtl number, $C_p \mu / k$
v	volumetric flow rate ($\mathrm{m^3/s}$) or (l/h)
Q	heat (kW)
q	heat flux ($\mathrm{kW/m^2}$)
Re	Reynolds number
R_t	mean roughness height (μm)
T	temperature (K)
u	velocity
We	Weber number

Greek symbols

$\dot{v}$	volumetric flow rate ($\mathrm{m^3/s}$)
μ	dynamic viscosity (Kg/m s)

Δp	pressure drop (kPa)
α	spray angle
ρ	density (kg/m^3)
σ	surface tension (N/m)
ω	Angular velocity (Hz)
δ	liquid film thickness (m)

Subscripts

am	ambient
at	atmospheric
ch	chamber
c	coolant
d	droplet
f	liquid phase
v	vapor phase
V	vibration
g	gas side
h	heater
H	heater surface
i	inner
l	liquid
lat	latent
m	modified
o	orifice
Ref	Refrigerant
s	surface
sat	saturation
sen	sensible
sub	subcooling
w	Wall

LIST OF FIGURES

LIST OF TABLES